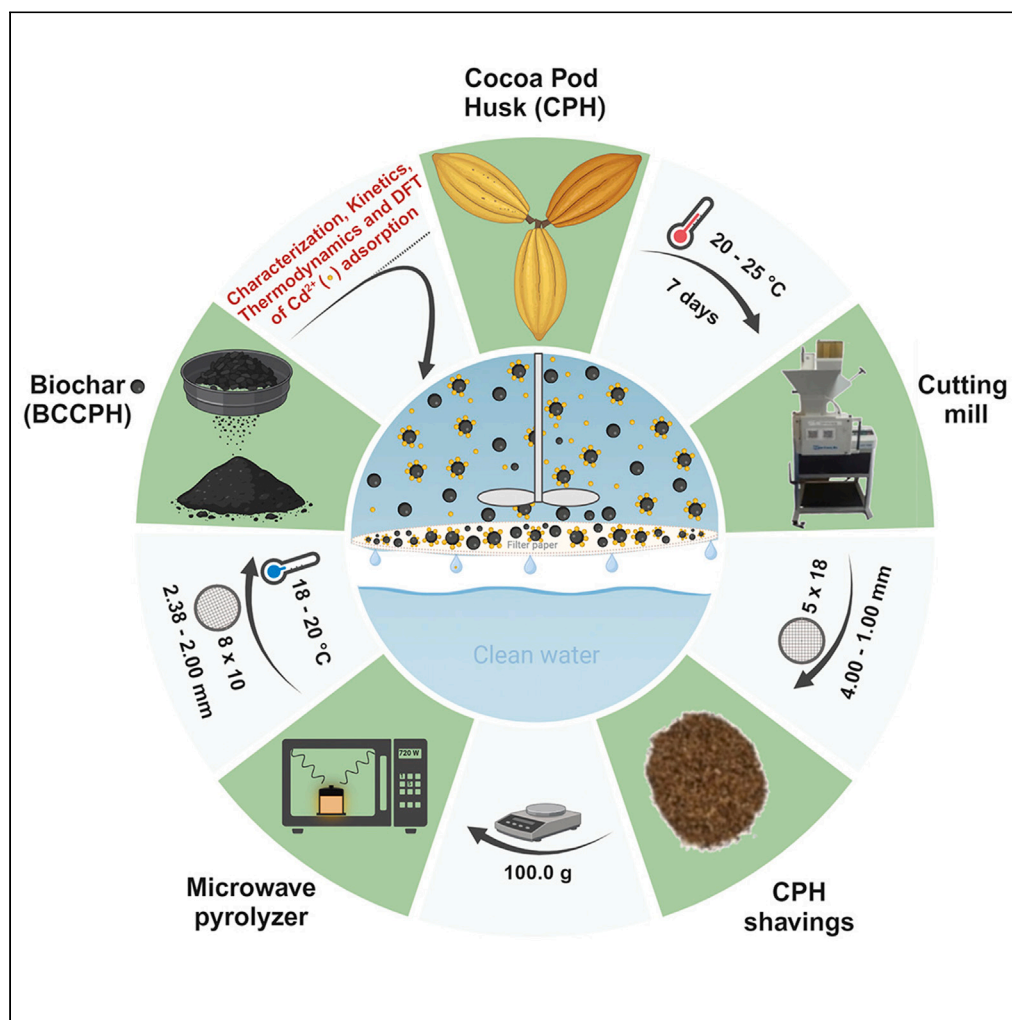Article

Adsorption dynamics of Cd^{2+}(aq) on microwave-synthetized pristine biochar from cocoa pod husk: Green, experimental, and DFT approaches

Jhonny Correa-Abril, Ullrich Stahl, Elvia V. Cabrera, ..., Sonia Taamalli, Florent Louis, Joan Manuel Rodríguez-Díaz

molemater@uce.edu.ec

Highlights

Microwave-synthetized biochar at 720 W/15 min has favorable adsorption performance

The pristine biochar (BCCPH) removes Cd^{2+}(aq) predominantly by physisorption

Oxygenated functional groups in BCCPH influence its adsorption mechanism

According to DFT, Cd^{2+} tends to bind to carbon atoms in the carbonaceous surface

Article

Adsorption dynamics of Cd^{2+}(aq) on microwave-synthetized pristine biochar from cocoa pod husk: Green, experimental, and DFT approaches

Jhonny Correa-Abril,[1,4] Ullrich Stahl,[1] Elvia V. Cabrera,[1] Yonathan J. Parra,[2,6,*] Michael A. Vega,[1,2] Sonia Taamalli,[3] Florent Louis,[3] and Joan Manuel Rodríguez-Díaz[5]

SUMMARY

Biochar obtained via microwave-assisted pyrolysis (MAP) at 720 W and 15 min from cocoa pod husk (CPH) is an efficient adsorbent of Cd^{2+}(aq). Biochar of residual biomass of CPH (BCCPH) possesses favorable physicochemical and morphological properties, featuring a modest surface area yet a suitable porous structure. Adsorption, predominantly governed by physisorption, is influenced by the oxygen-containing active sites (-COOR, -C(R)O, and -CH$_2$OR; R = H, alkyl). CdCO$_3$ formation occurs during adsorption. Experimental data were well-fitted into various kinetic models for a broad understanding of the sorption process. Langmuir model indicates a maximum adsorption capacity of 14.694 mg/g. The thermodynamic study confirms the spontaneous and endothermic sorption. Studies at the molecular level have revealed that the Cd^{2+} ion tends to bind to surface aromatic carbon atoms. This sustainable approach produces BCCPH via MAP as a solution for waste transformation into water-cleaning materials.

INTRODUCTION

Usually, agricultural production to satisfy the demand of the population is increased by applying high amounts of synthetic fertilizers, which in turn causes high nitrate levels in the groundwater[1] and phosphate fertilizers that generate contamination with cadmium (Cd) due to the presence of Cd minerals in the phosphorite and apatite rocks used in the production of these fertilizers.[2–7] Heavy metals such as Cd can contaminate irrigation waters, either naturally or due to human activities. When these contaminated waters are used for irrigation, the metals get absorbed by the soil, thus increasing their concentration in the soil.[8] Consequently, plants growing in such soil absorb these metals, making them bioavailable for people through the parts agriculturally used, like fruits and seeds.[9,10] A common strategy nowadays used to circumvent this problem is the application of higher amounts of competing elements, such as silicon or zinc, to the roots of the plants to minimize the uptake of heavy metals like Cd.[11,12]

Cd exposure occurs by eating contaminated foods.[13] It accumulates in organs such as the liver, heart, kidneys, and brain, disrupting normal biological functions.[14–18] High urine Cd levels are associated with increased mortality.[19,20] Thus, finding solutions to address Cd pollution control is imperative.

Adsorption processes as sustainable processes for capturing heavy metals in contaminated waters, and soils are a globally applicable strategy.[21–25] Biochar is an alternative and cost-effective material that can remove heavy metals from water by different mechanisms that happen on the carbonaceous surface, e.g., physical interactions, H-bond interactions, complexation, or co-precipitation, to name a few.[26] This biomaterial is prepared through conventional[27,28] and microwave[29,30] processes, the latter being advantageous because it requires less time for production, allows rapid and uniform heating, is a more precisely controllable process, and has the possibility of reducing secondary reactions, which leads to the reduction of gaseous emissions.[31]

The waste revalorization of the abundant biomass of the cocoa pod husk (CPH) would be its conversion to biochar via microwave-assisted pyrolysis (MAP) to improve the properties of the soils and water at a low cost, as already proposed by the slash-and-char principle.[21,32] Important research has focused on studying methods of modifying biochar to improve its adsorption capabilities and applications for treating

[1]Universidad Central del Ecuador, Facultad de Ingeniería Química, Grupo de Investigación en Moléculas y Materiales Funcionales (MoléMater), Enrique Ritter s/n y Bolivia, Quito, Pichincha 170521, Ecuador
[2]Universidad Central del Ecuador, Facultad de Ingeniería en Geología, Minas, Petróleos y Ambiental, Grupo de Investigación en Moléculas y Materiales Funcionales (MoléMater), Jerónimo Leyton y Gilberto Gatto Sobral, Quito, Pichincha 170521, Ecuador
[3]Université de Lille, CNRS, UMR 8522, PhysicoChimie des Processus de Combustion et de l'Atmosphère – PC2A, 59000 Lille, France
[4]Facultad de Posgrado, Universidad Técnica de Manabí, Av. Urbina y Che Guevara, Portoviejo, Manabí 130104, Ecuador
[5]Laboratorio de Análisis Químicos y Biotecnológicos, Instituto de Investigación, Universidad Técnica de Manabí, Av. Urbina y Che Guevara, Portoviejo, Manabí 130104, Ecuador
[6]Lead contact
*Correspondence: molemater@uce.edu.ec
https://doi.org/10.1016/j.isci.2024.109958
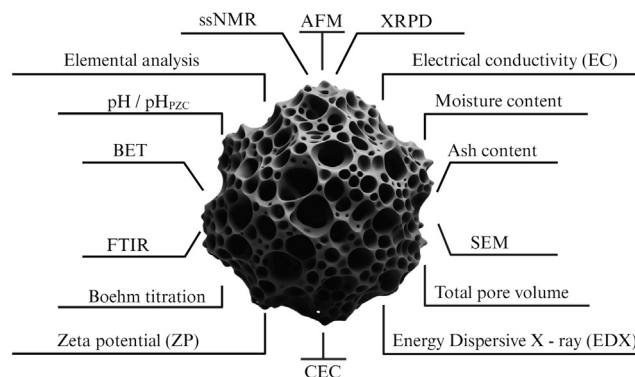
Figure 1. A schematic overview of analytical techniques employed to understand the properties of the BCCPH

contaminated water and soils.[33,34] However, the preparation methods of modified biochar can be complicated and lengthy and require the use of additional chemicals.[35]

Ecuador is well known for its unique "Fino de Aroma" cocoa production. In its territory, about 509,000 ha are currently harvested, producing around 337,000 tons of cocoa-dried beans.[36] Of the whole fruit, only 20% resembles the valued cocoa beans, while the pod husks making up 75% of the fruit[37] are predominantly left to rot on the soil. The revalorization of the abundant waste during the cocoa harvest in Ecuador, which is a fundamental basis of its economy and whose waste generation leads to problems of bacterial or fungal contamination (*Phytophthora*) that causes substantial losses in the plantations and decreases production,[38,39] is imperative.

The novelty of the present study is based on producing biochar with this CPH waste to address several problems we are currently working on: 1) proposing a method to transform biomass into pristine biochar with appropriate pore structure through the use of microwave radiation, 2) the use of biochar for the adsorption of heavy metals such as Cd in water and soils, 3) application of biochar as a fertilizer in soils to improve crops, and as a carbon sequestrant for climate change mitigation, and 4) generating a circular economy, especially for small agricultural communities with few resources. The topic of this work is aligned with the Sustainable Development Goals Report 2023 by the United Nations,[40] which emphasizes the immense potential for the utilization of lignocellulosic biomass "contributing to create a brighter future for all" with a focus on goal number 6: clean water and sanitation.

The study of physical diffusion processes and chemical reactions at active sites is crucial for understanding adsorption mechanisms. This knowledge is essential for designing effective adsorbent materials, as heavy metals interact with functional groups such as carboxyl, hydroxyl, and carbonyl, as well as the aromatic carbonaceous surfaces. The first can be determined via sorption experiments and data analyzed through kinetic and chemical equilibrium mathematical models, while the latter are studied via density functional theory (DFT) calculations.[41,42]

This study had the following objectives: a) generation and characterization of biochar by MAP of residual biomass of CPH (BCCPH) and biochar with adsorbed Cd (BCCPH-Cd), b) determination of the experimental kinetic data of the adsorption process and analysis by various mathematical models, c) estimation of the equilibrium constants and thermodynamic parameters of the adsorption process, d) calculation of the Cd^{2+} adsorption energies on the carbonaceous surface using a DFT approach, and e) proposal of a possible mechanism of the Cd^{2+} ion adsorption process on the BCCPH.

RESULTS AND DISCUSSION

Physicochemical and morphological attributes of microwave-synthesized pristine biochar shape its adsorption potential

Various analytical techniques were utilized to gain insights into the textural, morphological, topographical, structural, and physicochemical properties of the BCCPH (Figure 1).

Yield, proximate analysis, and physicochemical properties

The proximate analysis was performed to analyze the biomass employed (CPH) and the quality of the biochar (BCCPH) obtained, as shown in Table 1. The raw CPH material mainly comprises cellulose, hemicellulose, lignin, and some inorganic compounds. The volumetric heating of CPH occurs by absorbing microwave radiation through the polar groups of the biomass, which try to orient themselves in the oscillating electromagnetic field. This movement causes friction between the molecules, leading to the observed heat. With this method, enough heat to pyrolyze CPH to obtain BCCPH can be produced. In test experiments, it was found that the optimal process parameters for producing BCCPH were 720 W of microwave power for 15 min.

The yield of BCCPH was 31.80%, comparable to the yield mentioned in the literature.[43,44] Comparing the results of CPH and BCCPH, the moisture content decreased from 13.28% to 4.83% and the volatile matter from 59.12% to 29.79%, indicating partial or incomplete pyrolysis. The fixed carbon content increased from 18.87% to 50.02%. The ash concentration increased from 8.83% to 14.68%.

Similar studies on the characterization of the CPH raw material have produced comparable results to those presented in this work. For example, Vaštyl et al. (2022)[45] obtained values of 40.0% and 17.1% by weight for elemental carbon and fixed carbon content, respectively,

Table 1. Characteristics of CPH and BCCPH

| Parameter	CPH	BCCPH[a]
Proximate analysis (wt. % by dry basis)		
Yield (%)	–	31.80 ± 1.49
Moisture (%)	13.28 ± 0.11	4.83 ± 0.02
Volatile (%)	59.12 ± 0.24	29.79 ± 0.83
Fixed carbon (%)	18.87 ± 0.33	50.02 ± 0.23
Total ash (%)	8.83 ± 0.33	14.68 ± 1.08
Physicochemical properties		
C (%)	41.08	63.99
H (%)	5.38	0.82
O (%)	51.54	33.95
N (%)	1.80	1.06
H:C	0.13	0.01
O:C	1.25	0.53
C:N	22.82	60.36
SSA (m^2/g)	–	2.83
Total pore volume (10^{-3} cm^3/g)	–	1.40
Average pore diameter (nm)	–	1.98
pH	5.67	11.06
pH_{PZC}	–	9.48
CEC (meq/100g)	232.33	281.60
EC (mS/cm)	–	8.89
ZP (mV)	–	−81.6

[a]MAP/720 W/15 min.

for CPH obtained from Peru. Ghysels et al. (2020)[46] in their study of the CPH from the province of Manabí (Ecuador), obtained 43.55% and 21.49% by weight for elemental carbon and fixed carbon content, respectively.

The elemental contents of CPH and BCCPH are presented in Table 1. The C content of the biomass increased through pyrolysis from 41.08% to 63.99%, while the O content decreased from 51.54% to 33.95%. This is due to the loss of volatiles, including CO_2 and H_2O. The atomic ratios of H:C, O:C, and C:N changed notably, suggesting that BCCPH was less oxidized and exhibited higher aromaticity than CPH, leading to a higher stability. Increased aromaticity and extended conjugated π-electron systems are essential for adsorbing heavy metals through surface complexation.[47]

The analysis of the surface of biochar with particle sizes ranging from 2.00 to 2.38 mm revealed that it had a Brunauer-Emmett-Teller (BET) specific surface area (SSA) value of 2.83 m^2/g and a total pore volume of 1.40 × 10^{-3} cm^3/g (Table 1), which is comparable with some values obtained in previous studies.[48,49] The content of ashes in the resulting biochar may hinder pore development during carbonization, which could explain the low values reported by BET analysis. BCCPH has an average pore diameter of 1.98 nm, which is approximately twice the diameter of a hydrated Cd ion (0.852 nm) and around 10 times the diameter of a bare Cd ion (0.194 nm).[50,51] These observations suggest that the micro-mesoporous structure[52] of the biochar is suitable for effectively adsorbing Cd ions in aqueous solutions. Despite its low surface area, the porous structure of the material is sufficiently large to allow the migration of Cd ions into the pores, which enhances the surface interaction and, therefore, the adsorption capacity of the biochar. Nevertheless, our study reveals that the adsorption capacity is governed not only by physical attraction but also by chemical interaction between the Cd ions and the oxygen-containing surface groups.

The pH of CPH was 5.67, while the pH of BCCPH was 11.06. This is because pyrolysis releases ashes, raising the pH.[53] This is confirmed by the values of electrical conductivity measured (8.89 mS/cm). In the literature, biochar electric conductivity (EC) values ranging from 0.04 mS/cm to 54.2 mS/cm have been reported.[54,55] The pH and the EC of biochar samples depend on the feedstock and the pyrolysis temperature. In general, higher pyrolysis temperatures produce higher EC values. This is attributed to the increasing concentration of residues or ash caused by the loss of volatile material during pyrolysis.[56,57] The cation exchange capacity (CEC) of biochar was 281.60 meq/100g, a value higher than that of the source biomass.[58]

An important parameter affecting the sorption capacity of the functional groups of the surface of BCCPH is the pH_{PZC}. If a solution has a pH lower than pH_{PZC}, the surface of BCCPH will turn the surface polarity to a positive charge, impeding the attraction and sorption of cations. Thus, selecting the optimal pH value for the adsorption experiments is essential to ensure an interaction between BCCPH and the cation to be
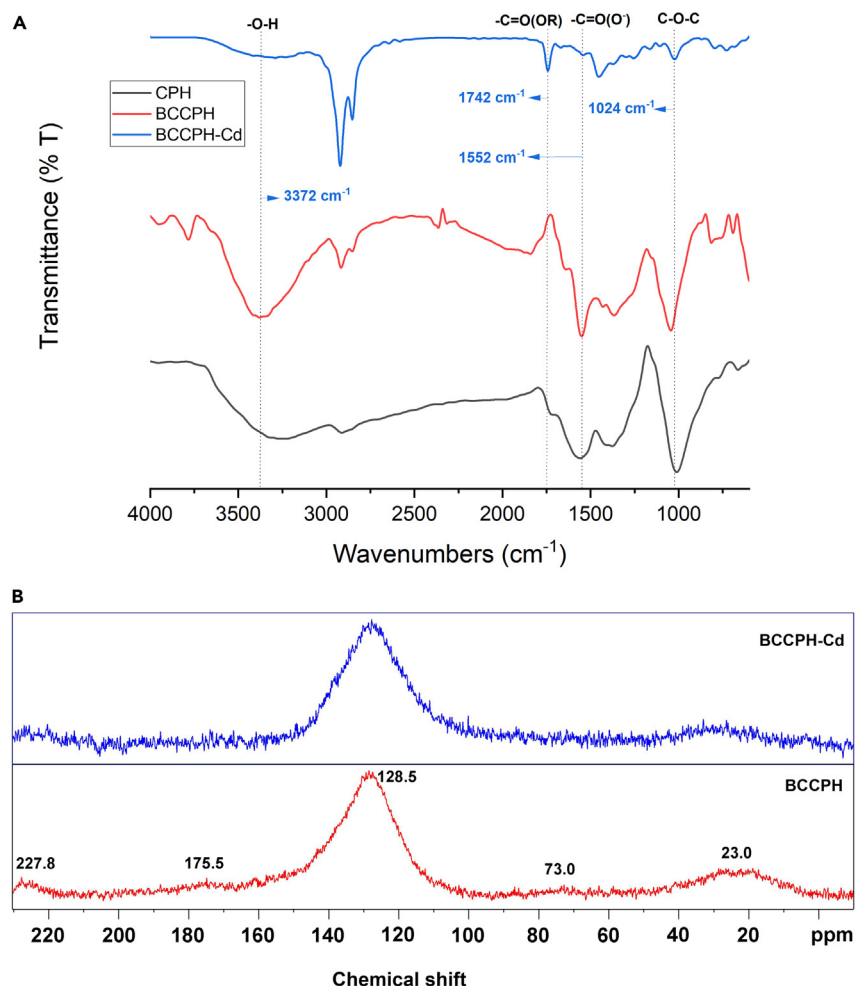
Figure 2. Functional group profile variations in the BCCPH during the adsorption of Cd^{2+}(aq)
(A) FTIR spectra of CPH, BCCPH, and BCCPH-Cd.
(B) ssNMR spectra of BCCPH and BCCPH-Cd.

adsorbed. Figure S1 shows the pH$_{PZC}$ value determined for BCCPH (9.48), which is in agreement with the results from Albalasmeh et al. (2020).[59]

The Zeta potential (ZP) measurements indicated that the surfaces of BCCPH were negatively charged, giving −81.6 mV (Figure S2). The value and sign of the ZP describe the surface charge of particles. The ZP results are negative when the surface charge is negative, as in the case of biochar with its accumulation of oxygen-rich functional groups. This behavior will aid in the adsorption of the positively charged Cd^{2+} and the stability of BCCPH in aqueous suspension.[60]

Since this work adopts an indirect method (back titration), the carbon surface functionality (CSF) can be calculated by applying the procedure of Ren et al. (2019).[61] The selective neutralization of different functional groups by different titrating bases enables the estimation of the functionalities of these groups by simply calculating the difference of the n_{CSF} estimated for different titrating bases (Table S1).

The results of the Boehm titration of BCCPH are shown in Table S2. A total acidity of 483.030 μmol/g can be separated into 246.540 μmol/g acidic groups and 236.490 μmol/g lactonic groups. There were no phenolic functional groups found. These data were corroborated by applying the direct titration methodology.[62] A study that can be used for comparison has shown that the total amount of oxygen-containing functional groups falls within the range of 470–490 μmol/g.[63]

FTIR and solid-state nuclear magnetic resonance analyses

The Fourier transform infrared (FTIR) spectra of CPH and BCCPH are compared with those of BCCPH subjected to a Cd^{2+} adsorption process (BCCPH-Cd) and are shown in Figure 2A. In the case of CPH, a peak at 1,731 cm^{-1} is observed, which is attributed to the stretching vibration of the carbonyl groups of the esters in pectin (acetyl and uronic), while the carboxylic acids in hemicellulose and lignin (ferulic and *p-coumarin*) are assigned to a broad peak at 1,552 cm^{-1}. The 1,320 cm^{-1} peak is attributed to the in-plane aromatic vibrations of the -C=C- bond of lignin

in conjunction with the out-of-plane = C-H bending peaks at 779 and 620 cm^{-1}. The broad peak at 1,011 cm^{-1} is due to pyranose's C-O-C bond stretching vibration. The peaks at 2,916 and 664 cm^{-1} are due to C-H stretching and bending vibrations. The broad peak with a maximum at 3,258 cm^{-1} corresponds to the vibration of the O-H group resulting from the inter- and intramolecular bonds of polymeric compounds such as carboxylic acids and alcohols, as well as the adsorbed water molecule.[64,65]

The FTIR spectra of BCCPH-Cd showed a change in frequency and an increase in peak intensity at 1,742 cm^{-1} which is due to the carboxylate groups of BCCPH possibly interacting chemically with the metal ions.[66] Moreover, it has been reported that the frequency shift of many functional groups after an adsorption process indicates the functional groups' interaction with metal cations.[67] On the other hand, a decrease in the peak intensity and peak width of the signals attributed to O-H and C-H bonds can be observed at 3,372 cm^{-1} and 2,918 cm^{-1} respectively, indicating that an interaction with hydroxyl groups might be occurring and that the adsorbent became more polar.[66] After treatment of the Cd^{2+} aqueous solution, the carboxylate group (-COO$^-$) vibration in the FTIR spectrum of BCCPH at 1,552 cm^{-1} practically disappeared, and the intensity of the stretching frequency of the C-O-C bond at 1,024 cm^{-1} decreased considerably.[64,65] This evidence suggests that these functional groups are likely active sites of adsorption.

In Figure 2B, the BCCPH shows signals associated with different chemical functional groups in the CPMAS ^{13}C-nuclear magnetic resonance (NMR) spectra:[68,69] 23.0 ppm (alkyl-C), 73.0 ppm (O-alkyl-C, ether/alcohol), 128.5 ppm (aryl-C), 175.5 ppm (carboxyl-C), and 227.8 ppm (carbonyl-C, aldehyde/ketone), while BCCPH-Cd experiences a disappearance of the bands at 73.0 ppm and 175.5 ppm and a decrease in band intensity to 227.8 ppm; this evidence suggests the involvement of alcohol/ether (-CH$_2$OR; R = H/alkyl), carboxylic acid/ester (-COOR), and aldehyde/ketone (-C(R)O) groups as active adsorption sites; respectively.

Surface morphology and topography

Scanning electron microscope (SEM) images of BCCPH and BCCPH-Cd are shown in Figure 3. It can be observed that the BCCPH has a sponge-like microporous structure (Figure 3A). At a magnification of 1,000x, one can see a fragile structure with steep walls and profound pores, apt for a good interaction between BCCPH and the Cd^{2+} ions (Figure 3B). This absorption behavior is depicted in Figure 3C, showing the Cd^{2+} sites in a pink color. These findings highlight how the specific porous configuration of the biochar compensates for its low surface area, facilitating a significant adsorption capacity for certain metallic contaminants in water.[70]

Topography refers to the physical attributes of a surface, such as its height, shape, and depth (Figure 3D). The area of interest under consideration has an image region size of 2.5 μm^2. Two parameters are employed to determine the roughness of the surface: mean roughness (Ra, nm) and standard deviation of the height value (Rq, nm). These parameters helped to characterize the surface topography of the biochar particle by measuring its set of surface irregularities (Figure 3E). Nanometric roughness was determined with Rq and Ra values of 63.506 and 51.953 nm, respectively. The following ranges can be considered to characterize the level of roughness: smooth (Ra <0.2 μm [200 nm]), medium-rough (Ra <0.4 μm [400 nm]), and rough (Ra >0.4 μm).[71] The analyzed biochar particle would be classified in the first group at the nanometer scale. However, microphotographs reveal subregions that go beyond depths of 100 nm, pointing to the presence of pores.

In Table S3 and Figure S3 the elemental composition, determined via SEM-energy-dispersive X-ray (EDX), is displayed before (BCCPH) and after the adsorption process (BCCPH-Cd). Apart from high values for C and O, K is present in quantities of 11.89 wt % before and 7.56 wt % after sorption, while Cd is present in 1.49 wt %. Figure S4 shows the EDX elemental mapping.

The X-ray powder diffraction (XRPD) (Figure 4A) revealed that a considerable part of BCCPH consists of non-crystalline carbonaceous matter. However, a semi-quantitative assessment of several crystalline phases was possible: 86% KHCO$_3$ (kalicinite), 10% CaCO$_3$ (calcite), and 4% CaC$_2$O$_4$·H$_2$O (whewellite). On the other hand, the XRPD of the BCCPH-Cd showed the presence of 28% CdCO$_3$ and 72% CaCO$_3$ (Figure 4B). The non-identification of KHCO$_3$ and the decrease of potassium (Table S3; Figure S3) on the surface of the biochar after the adsorption of Cd^{2+}(aq) ions suggest cation exchange and precipitation. The process can be explained by the ionic charge density (ρ). Cd^{2+} is a metal ion with a higher charge density than a K$^+$ ion.[72] Due to this, Cd^{2+} is more attracted to the negative charge of the HCO$_3^-$/CO$_3^{2-}$ species. As a result, Cd^{2+} replaces the K$^+$ ion.

Adsorption dynamics of Cd^{2+}(aq) onto BCCPH suggest favorable performance

The species distribution diagram for Cd^{2+} from Cd(NO$_3$)$_2$·4H$_2$O indicates that it precipitates at a pH higher than 8 (Figure S5). For this reason, the pH was set at a value of 5 to ensure that no precipitation of Cd^{2+} could happen.[73] Cd mainly existed in the form of Cd^{2+} in the studied pH range, thus resulting in competitive adsorption between H$^+$ and Cd^{2+}. The pH of the solution significantly affects surface properties such as the protonation of functional groups (-COOR, -C(R)O, and -CH$_2$OR at lower pH), causing an electrostatic repulsion between the cations and the positively charged surface. Considering that the pKa range of carboxylic acid groups is between 3 and 6, it is unlikely that protonation is total on the adsorbent surface. At higher pH, more negatively charged binding sites are created, promoting the attraction of adsorbed metal ions on adsorbents.[74]

Effect of BCCPH dosage

Figure S6 shows the adsorption percentage of a Cd^{2+} solution at different BCCPH dosages. The BCCPH dosage had an important effect on the adsorption of Cd^{2+}. Increasing the BCCPH dosage gradually stabilizes the removal percentage from 9% to 79%. This behavior occurred because the number of surface adsorption sites increased with higher doses of BCCPH, thus promoting the adsorption and increasing the removal rate of Cd^{2+}. At the experimental concentration, the optimal addition amount of biochar resulted in 1.5 g. At higher doses, the removal percentage does not vary significantly, indicating that the Cd^{2+} in the solution reached adsorption equilibrium. In contrast,
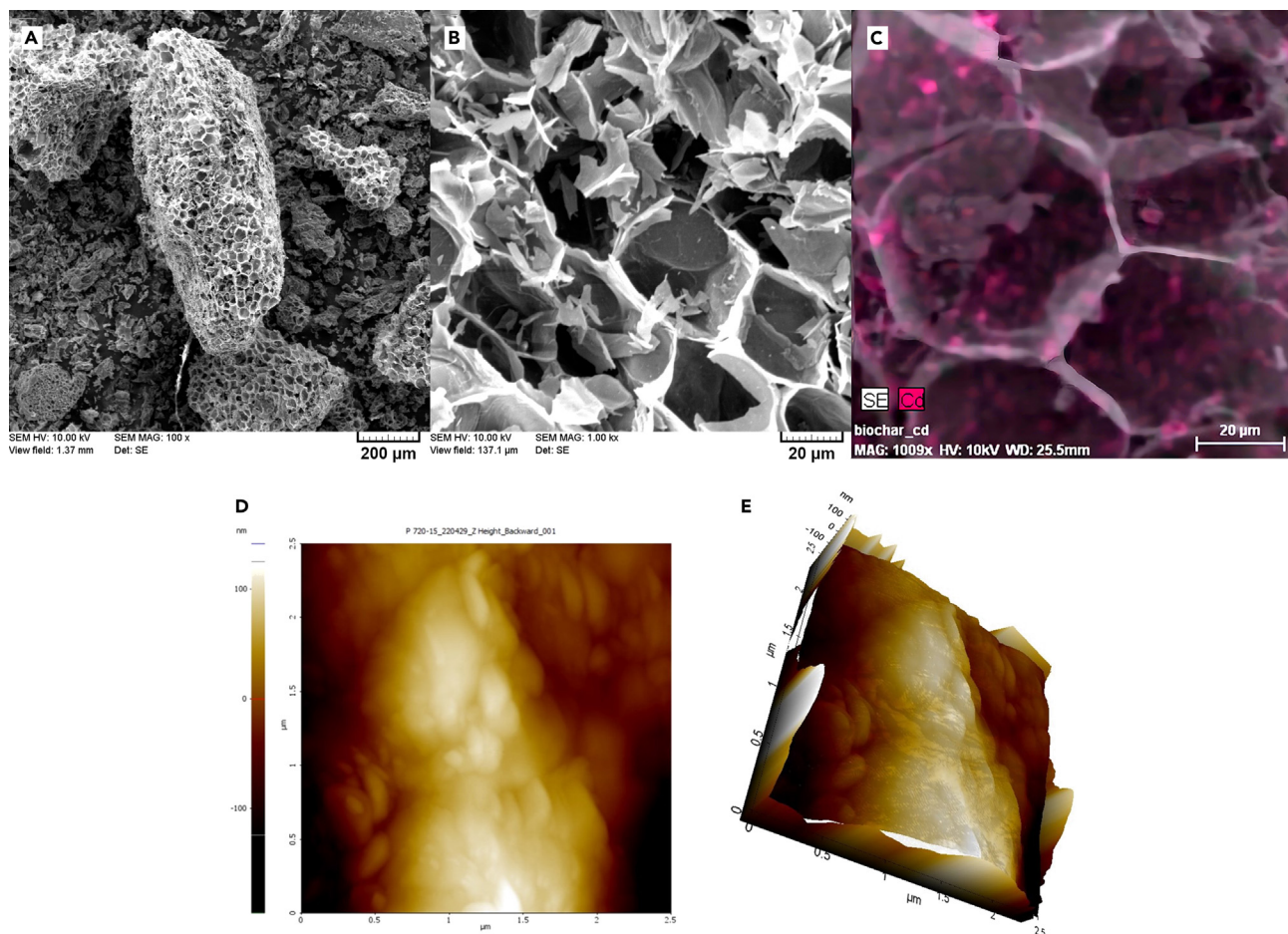
Figure 3. Microphotographs depict morphological and topographic properties of BCCPH, illustrating Cd adsorption

(A–C) SEM images of BCCPH at (A) 100x, (B) 1,000x magnifications before adsorption, and (C) after Cd adsorption (highlighted with pink dots). See also Table S3, Figures S3 and S4.

(D and E) Atomic force microscopy (AFM) images of BCCPH showing (D) phase contrast – 2D for surface homogeneity and (E) surface topography – 3D for microstructure, valleys, and peaks.

the adsorption capacity decreased from 8.57 mg/g to 2.33 mg/g, as observed in Figure S6. This may be caused by excessive adsorbent dosage, which results in agglomeration of the BCCPH particles, causing overlap of the adsorption sites and blocking the diffusion of Cd^{2+}, which in turn reduces the adsorption capacity.[75]

Adsorption kinetics, equilibrium isotherms, and thermodynamic parameters

The experimental adsorption kinetics data adjustment results using Boyd's external diffusion models (Figure 5A) and Weber-Morris (Figure 5B) provide information on diffusive physical processes. As shown in Figure 5A, the plot is linear. Still, it does not pass through the origin, suggesting that external diffusion or both external and intraparticle diffusion governs the overall rate of the sorption process. This is shown in Figure 5B, where the plot shows multiple straight lines, indicating that external diffusion and pore diffusion seem to happen simultaneously. However, the effective diffusion coefficient, whose value is in the order of 10^{-7} (Table 3), indicates that external diffusion should be the predominant mass transfer step. Then, the adsorption process happens to a greater extent at the initial stage (Figure 5B), showing an adsorption capacity of 4.98 mg/g, at a time equal to 5 min. This represents about 79% of the value of the adsorption capacity at equilibrium (q_e = 6.31 mg/g). Removal of 72% of the Cd ions present in solution is achieved in a short period of time (Figure S7). These results indicate that the BCCPH obtained by MAP is a good prospect for removing heavy metals from aqueous solutions.

Table 2 presents a comparison of the adsorption capabilities of the biochar produced from CPH using the MAP technique in this study, with those obtained from other types of charcoals produced from CPH through pyrolysis in a muffle furnace, as reported in the scientific literature. The findings reveal that, overall, the BCCPH produced using microwaves exhibits comparable or better adsorption properties than those obtained through conventional pyrolysis methods. These results suggest that microwave pyrolysis is a promising approach to biochar production.[76]
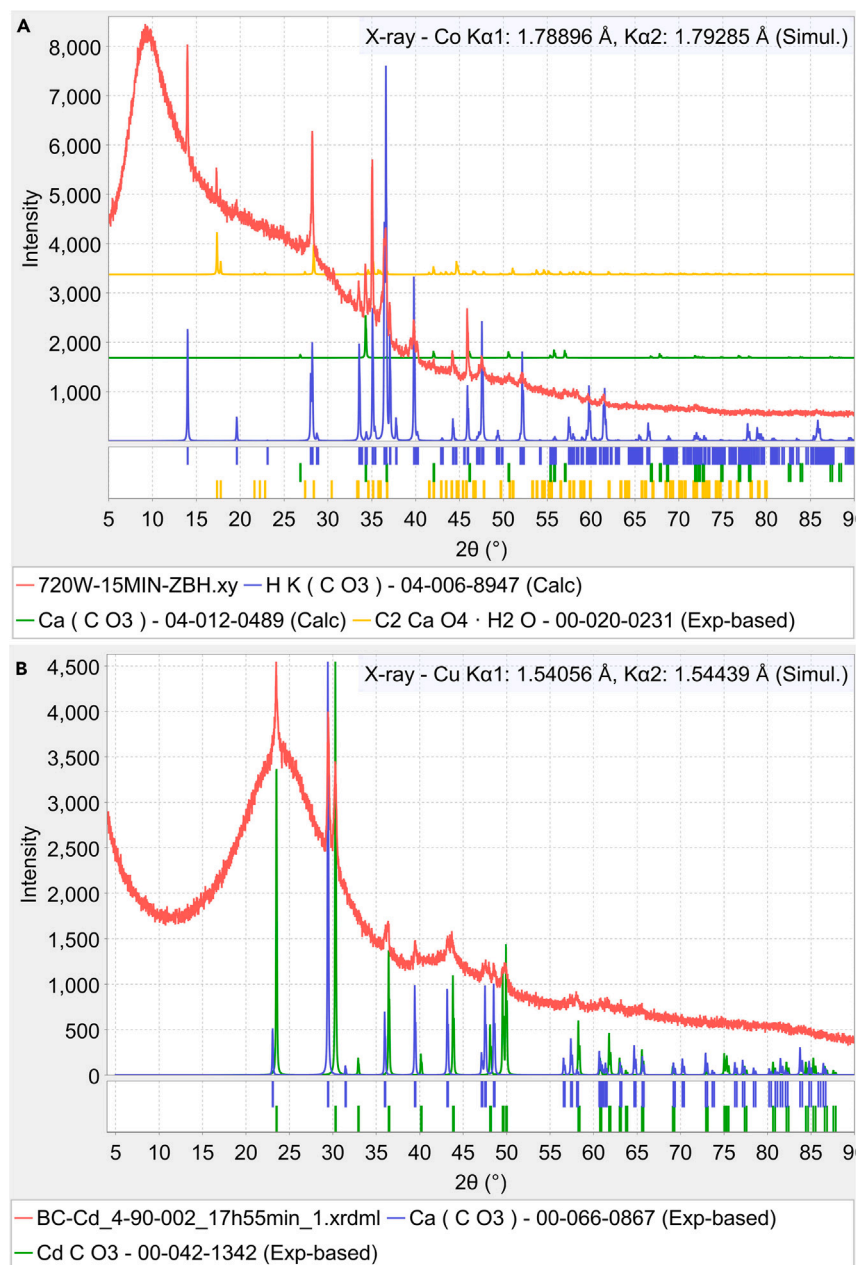
Figure 4. Crystalline phase analyses reveal mineralogical changes on the BCCPH surface and their potential impact on Cd adsorption

(A) XRPD pattern of BCCPH at 720 W-15 min before adsorption of Cd.

(B) XRPD pattern of BCCPH at 720 W-15 min after adsorption of Cd.

Figure 5C shows that the best-fitting mathematical model corresponds to Elovich kinetic ($\Delta q_e = 0.06$ mg/g, adjusted $R^2 = 0.999$, $Chi^2 = 0.005$), suggesting that the active sites are different and the activation energy increases with the adsorption time. This is explained by alcohol/ether, carboxylic acid/ester, aldehyde/ketone, and lactone functional groups (Figure 2B; Table S2) and the possible involvement of aromatic carbon atoms as potential active sites. Also, Ritchie kinetics reveals that each Cd ion needs between 1.7 and 2 active sites at the chemical adsorption step. Moreover, the excellent fit of the experimental data with the pseudo-second-order (PSO) model indicates that in the final step of the adsorption process, the fraction of active sites occupied in the adsorbent is abundant, with approximately 1.027×10^{20} active sites per square meter (calculated from Table S2). The high values of the rate constants (Table 3) related to chemisorption reveal the instantaneous adsorption of this step. Finally, the pseudo-first-order (PFO) model also presented acceptable statistical figures of
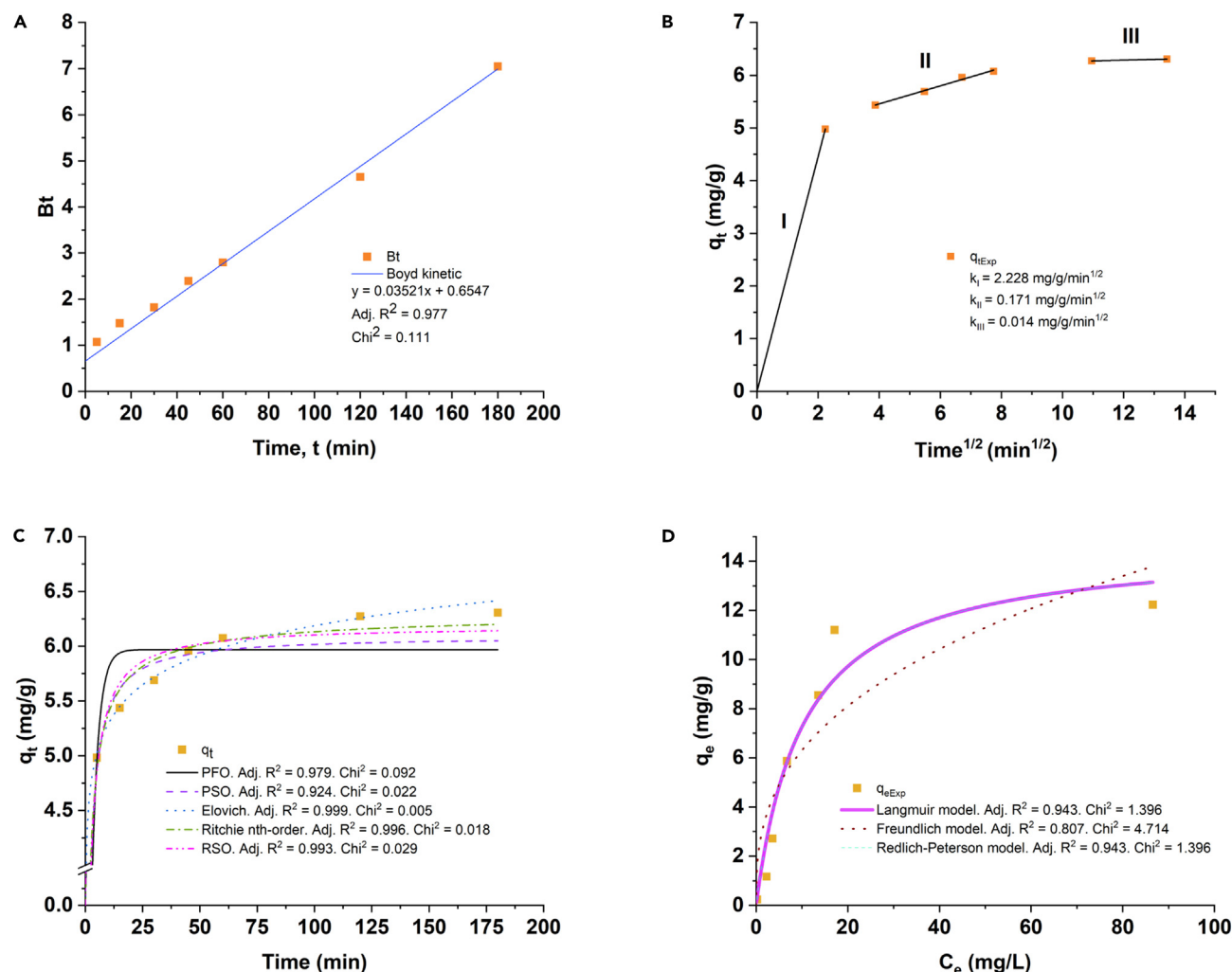
Figure 5. Exploring adsorption dynamics: using various well-fitted models to understand Cd^{2+}(aq) adsorption onto BCCPH

(A–C) (A) Boyd plot, (B) intraparticle diffusion plots, and (C) fitting curves of the adsorption kinetics of 100 mg/L Cd^{2+}(aq) onto BCCPH. See also Figures S5–S7.
(D) Adsorption isotherms of Cd^{2+} onto BCCPH: Langmuir, Freundlich, and Redlich-Peterson models. BCCPH = 1.5 g, Vol. Cd^{2+}(aq) = 100 mL, T = 293 K. See also Tables S4 and S5, and Figure S8.

merit as well as a $\Delta q_e = 0.34$ mg/g, reaffirming that the adsorption process occurs predominantly at the initial step, where few active sites are occupied because at this early stage of the physical process mass transfer phenomena are more important.

The adsorption isotherm curves shown in Figure 5D were fitted by the Langmuir, Freundlich, and Redlich-Peterson isotherm model, and the corresponding fitting parameters are listed in Table 4. It can be seen that the curves at the beginning present low equilibrium adsorption capacities (q_e) and, as the equilibrium concentration (C_e) increases, the adsorption capacity also increases. Thus, it was determined that the best-fitting nonlinear mathematical model is the Langmuir model ($\Delta q_e = 0.47$ mg/g, adj. $R^2 = 0.953$, Chi$^2 = 1.396$), which was corroborated by the Redlich-Peterson model. As the R_L value determined lies between 0 and 1, it suggests that the adsorption process on active sites is favorable. It can also be affirmed that the chemisorption is reversible in the BCCPH-Cd system since the Langmuir model assumes several important aspects: the surface is homogeneous, the system is saturated, the adsorption is reversible, the adsorption heat is independent of the degree of surface coverage, and all the sites are equivalent.[82,83]

The isotherm parameters for Langmuir at different temperatures, along with their corresponding equilibrium constant dimensionless values (calculated from Equation 22), are listed in Table S4. Values of parameters related to monolayer saturation, Q_{max}, increase with the rise of temperature, confirming the endothermic nature of the sorption process. The K_L parameter indicates the affinity for the binding of Cd^{2+} ions, and a high value of K_c obtained from K_L represents higher affinity by the active sites. The favorability of the adsorption process is also determined by the R_L parameter estimated using Equation 21; all the R_L values lie in the range of $0 < R_L < 1$, suggesting that the Cd^{2+} ions are favorably adsorbed on BCCPH.

Table 2. Efficiencies of different forms of charcoal derived from CPH for metal ion adsorption in water

Forms of charcoal	Conditions of preparation	Yield (%)	Particle size (mm), dosage (g)	Initial conc. (mg/L), M^{n+}(aq)	Contact time (min), rpm, pH.[a]	Adsorption capacity, qt (mg/g).[b]	Removal (%)	Reference
Biochar	MAP: 720 W, 15 min, without modification or pre-treatment.	31	2.38–2.00, 1.5	100, Cd^{2+}	60, 300, 5	6.08	87.88	In this work Figure S7
					120, 300, 5	6.27	90.74	
					180, 300, 5	6.31	91.22	
	PMF: 600°C, 10°C/min, 120 min.	27	N.R., 1.25	100, Cd^{2+}	240, 29, 9	3.89	97.15	Pinzon-Nuñez et al.[77]
	PMF: 500°C, 30 min, under limited O_2(g)	N.R.	2.00, 4	20, Cd^{2+}	60, 150, 4	0.49	99.99	Abbey et al.[78]
	PMF: 500°C, 10°C/min, 60 min, under N_2(g) flow.	N.R.	0.15, 1.5	25, Cr^{6+}	60, 400, N.R.	0.19	11.16	Aderonke et al.[79]
				25, Pb^{2+}	60, 400, N.R.	1.65	99.08	
Activated charcoal	PMF: 500°C, 10°C/min, 60 min, under N_2(g) flow. Post-activating.	N.R.	1.00–1.70, 2	3.56, Cu^{2+}	60, 1000, 6	0.05	58.15	Odubiyi et al.[80]
					120, 1000, 6	0.09	98.85	
				2.94, Pb^{2+}	60, 1000, 6	0.05	64.64	
					120, 1000, 6	0.07	99.01	
	Immersion with activating agent. PMF: 500°C, 15 min.	N.R.	0.30–0.45, 2.5	20, Cd^{2+}	150, 180, N.R.	0.40	98.92	Osakwe et al.[81]

[a]Temperatures in the adsorption experiments ranged from 293 to 305 K.
[b]Calculated by us from the reported experimental data. PMF, pyrolysis with muffle furnace; N.R., not reported.

The results shown in Figure S8 indicate that as the temperature increases, the adsorption capacity of the adsorbent experiences a very slight enhancement. This phenomenon can be attributed to the reduction in solution viscosity at elevated temperatures, leading to the rapid diffusion of Cd^{2+} ions from the liquid phase to the external boundary layer and surface cavities of the adsorbent particles. The high temperature promotes increased mobility of ions within the adsorbent, facilitating the formation of a monolayer over the active sites on the adsorbent's surface.[84] However, it should be noted that, although the increase in temperature may increase the mobility of ions, there may be other factors contributing to the negligible improvement in adsorption capacity with the increase in temperature. For example, if available adsorption sites are already widely occupied and if the rate at which ions bind to adsorption sites is relatively low, then the overall adsorption capacity cannot be significantly increased. Despite the aforementioned fact, these results suggest that the adsorption process is endothermic.

Table S5 shows the results obtained for the thermodynamic parameters. The Gibbs free energy (ΔG) decreases as the temperature increases, indicating that the adsorption process in the BCCPH-Cd system is spontaneous and thermodynamically stable. As for the enthalpy change (ΔH), the positive value was approximately 20 kJ/mol, indicating that the adsorption process is endothermic.[85] Previous research has reported that ΔH values for physical adsorption are less than 40 kJ/mol.[86,87] Therefore, the adsorption process of Cd^{2+} can be classified as physisorption, which is consistent with what was found in the kinetic studies described earlier. The positive value for the entropy change (ΔS) is indicative that there is a random increase at the solid/liquid interface when there is an increase in temperature and also that there is an increase in the degree of freedom of the adsorbed species and suggests some structural changes in BCCPH.[88]

DFT studies suggest surface carbon atoms of biochar as potential active adsorption sites
Modeling the carbonaceous surface

Studying the adsorption of Cd^{2+} on carbonaceous surfaces at a molecular scale is important to start establishing a model for the surface. In previous studies, the zigzag and armchair models were used in several studies with different applications to model carbonaceous surfaces.[89–92]

This study used the seven benzene rings as a zigzag model and four benzene rings as an armchair model. The spin multiplicity of the ground state was 3 for the armchair model and 6 for the zigzag model. The bond states between two atoms, and the Mulliken charges of atoms were obtained while doing geometry optimizations. Therefore, edge atoms at the model's top are unsaturated to simulate active carbon sites, while other edge carbons are terminated with hydrogen atoms.

Figure 6A shows the structure of two types of carbon models; the first one has a zigzag structure, while the other one has an armchair configuration. To facilitate the discussion in the following, some carbon atoms have been labeled. Note that the π-bond network is implied

Table 3. Kinetic fitting parameters for adsorption of Cd^{2+} onto BCCPH at 293 K

| Kinetic model	Parameter	Value
Models of diffusion		
External diffusion of Boyd	B_t (1/s)	$5.868 \times 10^{-4} \pm 0.0000$
	D_l (cm^2/s)	$5.946–8.419 \times 10^{-7}$
	Adj. R^2	0.977
	Chi^2	0.111
Weber and Morris or intraparticle diffusion	k_I (mg/g/$min^{1/2}$)	2.228 ± 0.000
	C_I (mg/g)	0
	R^2	1
	Chi^2	0
	k_{II} (mg/g/$min^{1/2}$)	0.171 ± 0.012
	C_{II} (mg/g)	4.773 ± 0.074
	R^2	0.985
	Chi^2	0.012
	k_{III} (mg/g/$min^{1/2}$)	0.014 ± 0.000
	C_{III} (mg/g)	6.125 ± 0.000
	R^2	1
	Chi^2	0
Models on active sites		
Ritchie nth-order ($n \neq 1$)	n	1.7 ± 0.0
	α (g^{n-1} mg^{1-n}/min)	2.001 ± 0.352
	q_e (exp), (mg/g)	6.31
	q_e (calc), (mg/g)	6.33 ± 0.08
	Adj. R^2	0.996
	Chi^2	0.018
Ritchie second-order ($n = 2$), (RSO)	α (g/mg/min)	0.717 ± 0.132
	q_e (calc), (mg/g)	6.19 ± 0.09
	Adj. R^2	0.993
	Chi^2	0.029
Empirical models		
Pseudo-first-order (PFO)	k_1 (1/min)	0.351 ± 0.063
	q_e (calc), (mg/g)	5.97 ± 0.12
	Adj. R^2	0.979
	Chi^2	0.092
Pseudo-second-order (PSO)	k_2 (g/mg/min)	0.128 ± 0.002
	q_e (calc), (mg/g)	6.09 ± 0.01
	Adj. R^2	0.924
	Chi^2	0.022
Elovich	α (mg/g/min)	31108.120 ± 26087.281
	β (mg/g)	2.569 ± 0.154
	q_e (calc), (mg/g)	6.25
	Adj. R^2	0.999
	Chi^2	0.005

in the figure. The models presented in Figure 6A reasonably represent the active site environment. The complete optimization of the geometry, i.e., the optimization of all atoms, is performed. All optimizations end with a minimum on the potential energy surface, indicating the stability of the carbon surface models we selected.[93]

Table 4. Isotherm fitting parameters for adsorption of Cd^{2+} on BCCPH at 293 K

Equilibrium model	Parameter	Value
Langmuir	q_e (exp), (mg/g)	6.31
	q_e (calc), (mg/g)	5.84
	K_L (L/mg)	0.098 ± 0.029
	Q_{max} (mg/g)	14.694 ± 1.594
	R_L (dimensionless)	0.097
	Adj. R^2	0.943
	Chi^2	1.396
Freundlich	q_e (calc), (mg/g)	5.47
	K_F (mg/g/(mg/L)^n)	2.736 ± 0.901
	n	0.362 ± 0.091
	Adj. R^2	0.807
	Chi^2	4.714
Redlich-Peterson	q_e (calc), (mg/g)	5.84
	b_{RP} (L/mg)	0.098 ± 0.029
	q'_{mon} (mg/g)	14.694 ± 1.594
	α (dimensionless)	1
	Adj. R^2	0.943
	Chi^2	1.396

Cd^{2+} adsorption on carbonaceous surface

Since there are several active sites for Cd^{2+} adsorption on the carbonaceous surface, the adsorption of Cd^{2+} at different initial sites on the zigzag and armchair models of the carbon surface was studied. According to the Mulliken charge, there are three Cd adsorption sites, C(6),
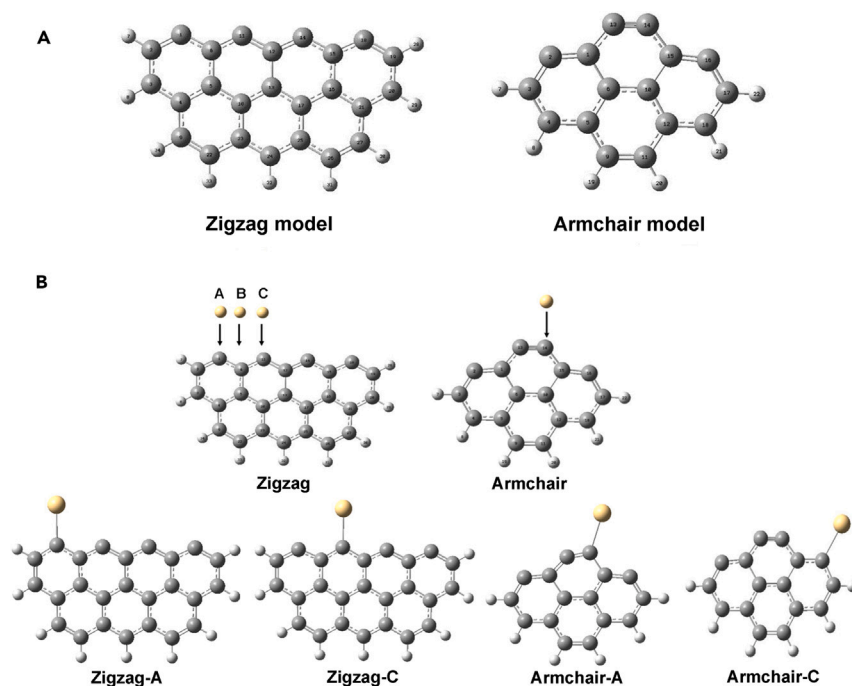
Figure 6. Theoretical surface carbon structures hint at potential Cd^{2+} adsorption sites
(A) Carbonaceous surface models.
(B) Adsorption sites of Cd^{2+} of each model.

Table 5. C–Cd bond lengths and adsorption energies of Cd^{2+} adsorption on the carbonaceous surface

Model	C$_{Ar}$–Cd experimental bond length (Å)[a]	C$_{Ar}$–Cd calculated bond lengths (Å)	E$_{ads}$ (kJ/mol)
Zigzag-A	2.151 ± 0.037	2.186	−105.29
Zigzag-C		2.177	−113.71
Armchair-A		2.184	−95.37
Armchair-C		2.309	−38.62

[a]Mean value ± SD of C$_{Ph}$-Cd bond lengths present in 39 of 43 crystal structures deposited in the Cambridge Structural Database (CSD) containing this type of bond, where a search was performed using ConQuest version 2023.3.0 software.[94]

C(11), and C(12), on the zigzag model and two sites, C(14) and C(16), on the armchair model as shown in Figure 6B. After the geometry optimization and vibrational frequency calculation, the structure of the carbon-Cd^{2+} complex was obtained. The different sites of Cd^{2+} on the zigzag and armchair shapes are shown as "A", "B," and "C." Both initial structures "B" and "C" led to the same optimized structure named zigzag-C, and "A" formed the structure zigzag-A.

Table 5 gathers optimized C–Cd bond lengths and corrected adsorption energies. As shown in Table 5, Cd^{2+} had a greater adsorption tendency to the zigzag surface. The adsorption energy of Cd^{2+} on zigzag-C was slightly higher than that of zigzag-A, which indicates that zigzag-C is the primary binding mode for the adsorption of Cd. This suggests that the structure of the zigzag-C-Cd^{2+} complex was more stable than the zigzag-A-Cd^{2+} complex. The armchair-A model had more negative adsorption energies than the armchair-C model. It is worth noticing that the adsorption of Cd^{2+} on the armchair-C configuration corresponds to a physisorption process, while all other reactions are chemisorption.
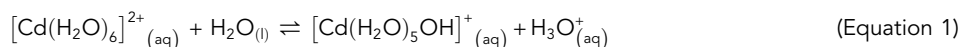
Proposal of the mechanism of Cd^{2+}(aq) removal by BCCPH: Understanding and insights

In general, in this study, kinetic mathematical models presented acceptable statistical figures of merit ($\Delta q_e < 0.35$, adjusted $R^2 > 0.900$, Chi$^2 < 0.12$); we decided on an eclectic approach where the physical meanings, chemicals, and conditions of these models are considered to propose a possible mechanism of removal of Cd ions in aqueous solution by BCCPH (Figure 7). Mass transfer in porous adsorbent materials is a complex process due to multiple mechanisms dependent on the adsorbent morphology and the abundance and availability of active sites. Many amorphous adsorbents, such as biochars, have a wide distribution of pore sizes and volumes (macro-, meso-, and microporous), making it difficult to determine the relative contribution of diffusion throughout the sorption process.[95] Therefore, here we consider that the kinetics of the process of removal of Cd ions by BCCPH have contributions of physisorption (diffusion) and chemisorption (adsorption on active sites).

Mass transfer phenomena by diffusion processes seem to be dominant. It is acceptable to think that the step that controls the rate of adsorption of Cd ions in solution by the BCCPH corresponds to the external diffusion (*ii*, Figure 5A; Table 3), where the driving force is the high adsorbate concentration gradient that exists between the adsorbent surface (low C$_o$: 0 ppm) and the liquid solution film that is around the adsorbent particle (high C$_o$: 100 ppm). The next step of the process (*iii*) has a relative contribution but does not seem to be the step that controls the kinetics of the global sorption process (Figure 5B). In addition, it is established that at a time equal to 5 min (region I, Figure 5B) the equilibrium in the intraparticle diffusion is reached by observing a higher value of k$_I$ (2.228 mg/g/min$^{1/2}$) with respect to k$_{II}$ and k$_{III}$ due to the ionic concentration gradient between the adsorbent surface and the most accessible pores within the adsorbent. Thus far, the predominance of diffusional physical processes is supported by the PFO kinetics usually applied for pure physical adsorption processes, which yield a low rate constant value (k$_1$ = 0.351 1/min). The experimental conditions in the adsorption tests fit well with the PFO model:[96] high C$_o$ of adsorbate, the adsorption process happens to a greater extent at the initial stage, and the adsorbent material has a few occupied active sites possibly because they are not available or accessible, due to the protonation of carboxylic acid/ester, aldehyde/ketone, and hydroxyl/ether functional groups which is favored by the experimental pH of 5.0 (pH$_{dissolution}$ < pH$_{PZC}$), causing the adsorbent surface to acquire partially a positive charge.

The last step (*iv*) of the sorption process happens once the equilibrium in the intraparticle diffusion in the pores is reached; the Cd ions are transferred very quickly to the activated sites, involving cation exchange, electrostatic attraction, and coordinate bond between the metal ion and a lone pair of electrons, among others (chemisorption). The instantaneous rate was confirmed by high kinetic constant values related to chemisorption (PSO: 128,000; Ritchie, *n* ≠ 1: 2,001,000; Ritchie, n = 2: 717,000; Elovich: 31,108; all in units mg/g/min) which turn out to be at least 88,000 times higher than the PFO (physisorption) rate constant.

The Cd^{2+} ion is easily hydrolyzed in water to give the equilibria shown in Equation 1 when [Cd^{2+}] < 0.1 M.[97] On the other hand, the number of active sites (n) ranges between 1.7 and 2 (Table 3), being reasonable to propose Equations 2, 3, and 4, where oxygenated groups are highlighted as active sites on the surface of the adsorbent. A coordination number equal to 6 is assumed for the Cd ion. Equation 5 represents the cation exchange that leads to the formation of Cd carbonate precipitate.
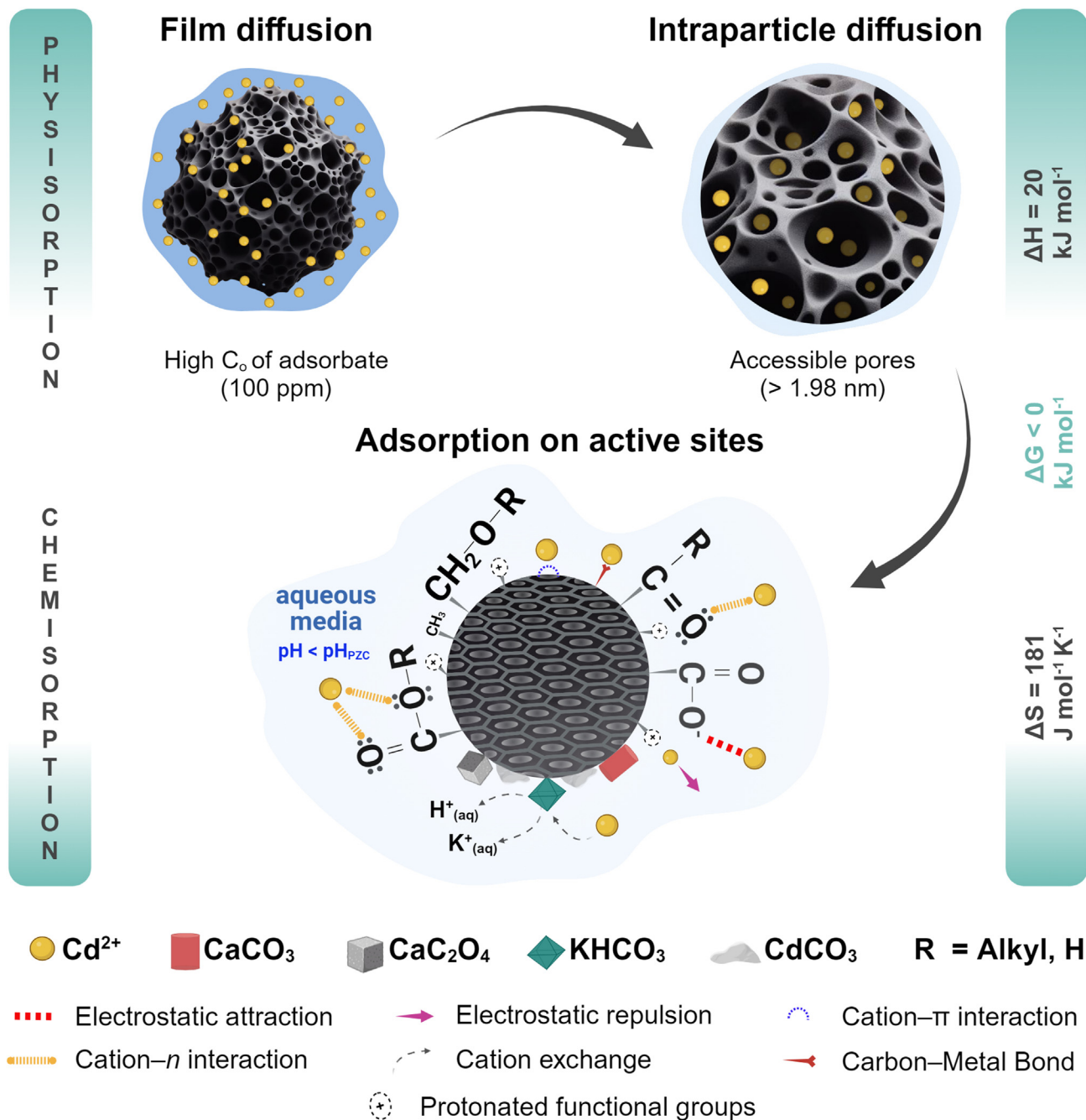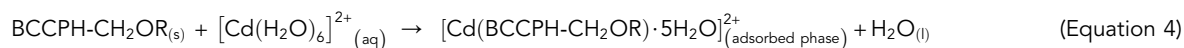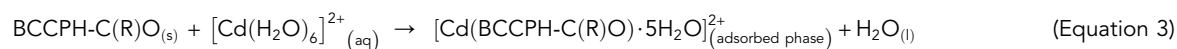
$$\left[Cd(H_2O)_6\right]^{2+}_{(aq)} + H_2O_{(l)} \rightleftharpoons \left[Cd(H_2O)_5OH\right]^{+}_{(aq)} + H_3O^{+}_{(aq)} \qquad \text{(Equation 1)}$$

Figure 7. Illustrating the probable mechanism of Cd²⁺(aq) adsorption by BCCPH

$$\text{BCCPH-COOR}_{(s)} + \left[\text{Cd}(\text{H}_2\text{O})_6\right]^{2+}_{(aq)} \rightarrow \left[\text{Cd}(\text{BCCPH-COOR})\cdot4\text{H}_2\text{O}\right]^{2+}_{(\text{adsorbed phase})} + 2\text{H}_2\text{O}_{(l)} \quad \text{(Equation 2)}$$

$$\text{BCCPH-C(R)O}_{(s)} + \left[\text{Cd}(\text{H}_2\text{O})_6\right]^{2+}_{(aq)} \rightarrow \left[\text{Cd}(\text{BCCPH-C(R)O})\cdot5\text{H}_2\text{O}\right]^{2+}_{(\text{adsorbed phase})} + \text{H}_2\text{O}_{(l)} \quad \text{(Equation 3)}$$

$$\text{BCCPH-CH}_2\text{OR}_{(s)} + \left[\text{Cd}(\text{H}_2\text{O})_6\right]^{2+}_{(aq)} \rightarrow \left[\text{Cd}(\text{BCCPH-CH}_2\text{OR})\cdot5\text{H}_2\text{O}\right]^{2+}_{(\text{adsorbed phase})} + \text{H}_2\text{O}_{(l)} \quad \text{(Equation 4)}$$

$$BCCPH@KHCO_{3(s)} + \left[Cd(H_2O)_6\right]^{2+}_{(aq)} \rightarrow BCCPH@CdCO_{3(s)} + K^+_{(aq)} + H_3O^+_{(aq)} \qquad \text{(Equation 5)}$$

Also, according to studies by DFT, it is plausible to consider the carbon atoms of the fused aromatic rings of the carbonaceous material as potential active centers. The overall process occurs spontaneously ($\Delta G < 0$ kJ mol^{-1}) and is endothermic ($\Delta H > 0$ kJ mol^{-1}).

Conclusions

This research conducted on the synthesis and characterization of pristine biochar from CPH via MAP has shown promising results, indicating its effectiveness as an adsorbent for Cd removal from aqueous environments.

Various analytical techniques have been employed to gain insights into the structural and chemical properties of BCCPH. Meanwhile, kinetic and equilibrium studies have provided valuable information about its adsorption performance. BCCPH is effective in removing Cd ions through two distinct phases. The initial phase is dominated by physisorption due to a high adsorbate concentration gradient and a porous size suitable for the diffusion of hydrated Cd ions within the adsorbent despite its modest surface area. The second phase involves chemisorption due to the presence of active sites, such as oxygen-containing functional groups that interact with Cd ions. This facilitates adsorption and allows them to bind more efficiently to the biochar. Experimental data fit into various kinetic models, and the Langmuir model indicates a maximum adsorption capacity of 14.694 mg/g at 293 K. DFT simulation suggested an organometallic chemisorption mechanism involving aromatic structures. Thermodynamic analysis has also suggested the spontaneity of the sorption process, highlighting the potential for practical applications in solid-liquid adsorption systems.

Overall, this comprehensive investigation solidified the potential of MAP as a green and facile method for producing BCCPH, a low-cost efficient adsorbent for addressing heavy metal pollution. These findings open new possibilities for contributing significantly to environmental sustainability and water purification applications, underscoring the importance of continued research and development in this area.

Limitations of the study

This study demonstrated the approach of using microwave radiation-assisted pyrolysis at 720 W and 15 min to synthesize BCCPH with morphological and physicochemical properties suitable for the adsorption and removal of Cd ions in synthetic polluted waters. However, the study has certain limitations that should be considered. First, the variability of BCCPH synthesis conditions is not addressed; a broader exploration of different synthesis parameters, such as microwave power and pyrolysis time, is needed to understand better how these variables affect biochar properties and adsorption capacity. Second, the results may not be completely generalizable to other pollutants or environmental conditions. Further studies would be useful to assess the efficacy of biochar in removing other heavy metals and in different aqueous matrices. Currently, we are addressing this variability of synthesis conditions and its implications on the properties of BCCPH in an additional study that will be presented in a forthcoming publication. Despite these limitations, the promising results of this study underscore the potential of microwave-synthetized pristine biochar and its application in the removal of contaminants in water. The importance of addressing these limitations is recognized in order to improve the understanding of the properties and performance of biochar obtained through MAP and its contribution to solving environmental problems.

STAR★METHODS

Detailed methods are provided in the online version of this paper and include the following:

- KEY RESOURCES TABLE
- RESOURCE AVAILABILITY
  - Lead contact
  - Materials availability
  - Data and code availability
- EXPERIMENTAL MODEL AND STUDY PARTICIPANT DETAILS
- METHOD DETAILS
  - CPH biomass preparation
  - Biochar preparation by MAP
  - Characterization of feedstock and biochar
  - Adsorption experiments
  - Computational details
- QUANTIFICATION AND STATISTICAL ANALYSIS

SUPPLEMENTAL INFORMATION

Supplemental information can be found online at https://doi.org/10.1016/j.isci.2024.109958.

ACKNOWLEDGMENTS

AUTHOR CONTRIBUTIONS

J.C.-A.: methodology, investigation, data curation, writing – original draft, writing & editing. U.S.: investigation, data curation, conceptualization, writing & editing, funding acquisition. E.V.C.: investigation, data curation, conceptualization, writing & editing. Y.J.P.: investigation, data curation, conceptualization, validation, visualization, writing – review & editing. M.A.V.: methodology, data curation, writing. S.T.: investigation, methodology, writing & editing. F.L.: investigation, methodology, writing & editing. J.M.R.-D.: supervision, methodology.

DECLARATION OF INTERESTS

The authors declare no competing interests.

REFERENCES

1. Zhang, Y., Chen, Z., Huang, G., and Yang, M. (2023). Origins of groundwater nitrate in a typical alluvial-pluvial plain of North China plain: New insights from groundwater age-dating and isotopic fingerprinting. Environ. Pollut. 316, 120592. https://doi.org/10.1016/j.envpol.2022.120592.

2. Kubier, A., and Pichler, T. (2019). Cadmium in groundwater — A synopsis based on a large hydrogeochemical data set. Sci. Total Environ. 689, 831–842. https://doi.org/10.1016/j.scitotenv.2019.06.499.

3. Marini, M., Caro, D., and Thomsen, M. (2020). The new fertilizer regulation: A starting point for cadmium control in European arable soils? Sci. Total Environ. 745, 140876. https://doi.org/10.1016/j.scitotenv.2020.140876.

4. Monika, M., Gupta, P.K., Singh, A., Vaish, B., Singh, P., Kothari, R., and Singh, R.P. (2022). A comprehensive study on aquatic chemistry, health risk and remediation techniques of cadmium in groundwater. Sci. Total Environ. 818, 151784. https://doi.org/10.1016/j.scitotenv.2021.151784.

5. Suciu, N.A., De Vivo, R., Rizzati, N., and Capri, E. (2022). Cd content in phosphate fertilizer: Which potential risk for the environment and human health? Curr. Opin. Environ. Sci. Health 30, 100392. https://doi.org/10.1016/j.coesh.2022.100392.

6. Khadim, M.U., Murtaza, G., Farooqi, Z.U.R., Hussain, T., Mahmood, N., and Hussain, S. (2023). An Application of Rock Phosphate Increased Soil Cadmium Contamination and Hampered the Morphophysiological Growth of Brassica campestris L. J. Soil Sci. Plant Nutr. 23, 4583–4595. https://doi.org/10.1007/s42729-023-01375-4.

7. Liu, Y., and Singh, B.R. (2024). Fate and behavior of cadmium in soils and recent advances in remediation technologies. In Inorganic Contaminants and Radionuclides (Elsevier), pp. 41–67. https://doi.org/10.1016/B978-0-323-90400-1.00012-4.

8. Orosun, M.M., Nwabachili, S., Alshehri, R.F., Omeje, M., Alshdoukhi, I.F., Okoro, H.K., Ogunkunle, C.O., Louis, H., Abdulhamid, F.A., Osahon, S.E., et al. (2023). Potentially toxic metals in irrigation water, soil, and vegetables and their health risks using Monte Carlo models. Sci. Rep. 13, 21220. https://doi.org/10.1038/s41598-023-48489-4.

9. Xiang, M., Li, Y., Yang, J., Lei, K., Li, Y., Li, F., Zheng, D., Fang, X., and Cao, Y. (2021). Heavy metal contamination risk assessment and correlation analysis of heavy metal contents in soil and crops. Environ. Pollut. 278, 116911. https://doi.org/10.1016/j.envpol.2021.116911.

10. Hu, Y., Wang, H., Zhou, B., Li, Z., Jia, H., Deji, P., Liu, N., and Wei, J. (2023). Effects of cadmium stress on fruits germination and growth of two herbage species. Open Life Sci. 18, 20220544. https://doi.org/10.1515/biol-2022-0544.

11. Khan, I., Awan, S.A., Rizwan, M., Ali, S., Hassan, M.J., Brestic, M., Zhang, X., and Huang, L. (2021). Effects of silicon on heavy metal uptake at the soil-plant interphase: A review. Ecotoxicol. Environ. Saf. 222, 112510. https://doi.org/10.1016/j.ecoenv.2021.112510.

12. Chen, F., Li, Y., Zia-Ur-Rehman, M., Hussain, S.M., Qayyum, M.F., Rizwan, M., Alharby, H.F., Alabdallah, N.M., Alharbi, B.M., and Ali, S. (2023). Combined effects of zinc oxide nanoparticles and melatonin on wheat growth, chlorophyll contents, cadmium (Cd) and zinc uptake under Cd stress. Sci. Total Environ. 864, 161061. https://doi.org/10.1016/j.scitotenv.2022.161061.

13. Satarug, S., Vesey, D.A., Gobe, G.C., and Phelps, K.R. (2023). Estimation of health risks associated with dietary cadmium exposure. Arch. Toxicol. *97*, 329–358. https://doi.org/10.1007/s00204-022-03432-w.

14. Seo, M.-N., Eom, S.-Y., Lim, J.-A., Lee, J.-E., Choi, B.-S., Kwon, H.-J., Hong, Y.-S., Kim, H., and Park, J.-D. (2023). Effects of Environmental Cadmium Exposure on the Liver in Korean Adults: Cross-Sectional and Longitudinal Studies. Arch. Environ. Contam. Toxicol. *84*, 237–247. https://doi.org/10.1007/s00244-023-00982-7.

15. Fu, M., Ren, Z., Liu, J., He, Y., Liu, C., Li, Y., and Cao, X. (2023). Association between cadmium exposure and the risk of cardiovascular outcomes: a meta-analysis. Hum. Ecol. Risk Assess. *29*, 1091–1108. https://doi.org/10.1080/10807039.2023.2236725.

16. Fujishiro, H., Sumino, M., Sumi, D., Umemoto, H., Tsuneyama, K., Matsukawa, T., Yokoyama, K., and Himeno, S. (2022). Spatial localization of cadmium and metallothionein in the kidneys of mice at the early phase of cadmium accumulation. J. Toxicol. Sci. *47*, 507–517. https://doi.org/10.2131/jts.47.507.

17. Ouyang, L., Li, Q., Rao, S., Su, R., Zhu, Y., Du, G., Xie, J., Zhou, F., Feng, C., and Fan, G. (2023). Cognitive outcomes caused by low-level lead, cadmium, and mercury mixture exposure at distinct phases of brain development. Food Chem. Toxicol. *175*, 113707. https://doi.org/10.1016/j.fct.2023.113707.

18. Li, C.-X., Talukder, M., Xu, Y.-R., Zhu, S.-Y., Zhao, Y.-X., and Li, J.-L. (2023). Cadmium aggravates the blood-brain barrier disruption via inhibition of the Wnt7A/β-catenin signaling axis. Environ. Pollut. *324*, 121400. https://doi.org/10.1016/j.envpol.2023.121400.

19. Laouali, N., Benmarhnia, T., Lanphear, B.P., and Oulhote, Y. (2023). Associations with Blood Lead and Urinary Cadmium Concentrations in Relation to Mortality in the US Population: A Causal Survival Analysis with G-Computation. Toxics *11*, 133. https://doi.org/10.3390/toxics11020133.

20. Shi, J.-W., Fan, D.-X., and Li, M.-Q. (2023). The Relationship between Cadmium Exposure and Mortality in Postmenopausal Females: A Cohort Study of 2001–2018 NHANES. Nutrients *15*, 4604. https://doi.org/10.3390/nu15214604.

21. Niu, L.Q., Jia, P., Li, S.P., Kuang, J.L., He, X.X., Zhou, W.H., Liao, B., Shu, W.S., and Li, J.T. (2015). Slash-and-char: An ancient agricultural technique holds new promise for management of soils contaminated by Cd, Pb and Zn. Environ. Pollut. *205*, 333–339. https://doi.org/10.1016/j.envpol.2015.06.017.

22. Dev, V.V., Nair, K.K., Baburaj, G., and Krishnan, K.A. (2022). Pushing the boundaries of heavy metal adsorption: A commentary on strategies to improve adsorption efficiency and modulate process mechanisms. Colloid Interface Sci. Commun. *49*, 100626. https://doi.org/10.1016/j.colcom.2022.100626.

23. Meng, Z., Huang, S., Laird, D.A., Wu, J., and Lin, Z. (2022). Identifying key processes driving Cd long-term adsorption and immobilization by biochar in soils and evaluating combined aging effects under simulated local climates. J. Environ. Chem. Eng. *10*, 108636. https://doi.org/10.1016/j.jece.2022.108636.

24. González Fernández, L.A., Navarro Frómeta, A.E., Carranza Álvarez, C., Flores Ramírez, R., Díaz Flores, P.E., Castillo Ramos, V., Sánchez Polo, M., Carrasco Marín, F., and Medellín Castillo, N.A. (2023). Valorization of Sargassum Biomass as Potential Material for the Remediation of Heavy-Metals-Contaminated Waters. Int. J. Environ. Res. Public Health *20*, 2559. https://doi.org/10.3390/ijerph20032559.

25. Miron, A., Neblea, I.E., Dolana, S.-V., Zaharia, A., Gavrilă, A.-M., Valente, A.J.M., Iordache, T.-V., and Chiriac, A.-L. (2023). Advanced Adsorbent Materials for the Remediation of Contaminated Waters with Heavy Metals via Enhanced Adsorption Mechanisms. NeXT-Chem *6*, 2023. https://doi.org/10.3390/proceedings2023090006.

26. Ambaye, T.G., Vaccari, M., van Hullebusch, E.D., Amrane, A., and Rtimi, S. (2021). Mechanisms and adsorption capacities of biochar for the removal of organic and inorganic pollutants from industrial wastewater. Int. J. Environ. Sci. Technol. *18*, 3273–3294. https://doi.org/10.1007/s13762-020-03060-w.

27. Gęca, M., Wiśniewska, M., and Nowicki, P. (2024). Preparation of biochars by conventional pyrolysis of herbal waste and their potential application for adsorption and energy purposes. ChemPhysChem *25*, e202300507. https://doi.org/10.1002/cphc.202300507.

28. Hayat, Z., Baig, S.A., Shams, D.F., Javed, H.A., Xu, X., and Danish, M. (2024). Insights into the effects of pyrolysis parameters on biochar synthesis from green wastes and its As(III) removal efficiency. Int. J. Environ. Sci. Technol. *21*, 895–908. https://doi.org/10.1007/s13762-023-05051-z.

29. Huang, Y.-F., Chiueh, P.-T., Kuan, W.-H., and Lo, S.-L. (2016). Microwave pyrolysis of lignocellulosic biomass: Heating performance and reaction kinetics. Energy *100*, 137–144. https://doi.org/10.1016/j.energy.2016.01.088.

30. Li, J., Lin, L., Ju, T., Meng, F., Han, S., Chen, K., and Jiang, J. (2024). Microwave-assisted pyrolysis of solid waste for production of high-value liquid oil, syngas, and carbon solids: A review. Renew. Sustain. Energy Rev. *189*, 113979. https://doi.org/10.1016/j.rser.2023.113979.

31. Reddy, B.R., Sarkar, S., and Vinu, R. (2023). Microwave-assisted rapid pyrolysis of woodblock without adding susceptor and detailed product analysis. Biomass Convers. Biorefin. 1–10. https://doi.org/10.1007/s13399-023-03820-x.

32. Samuel Olugbenga, O., Goodness Adeleye, P., Blessing Oladipupo, S., Timothy Adeleye, A., and Igenepo John, K. (2024). Biomass-derived biochar in wastewater treatment - a circular economy approach. Waste Manag. Bull. *1*, 1–14. https://doi.org/10.1016/j.wmb.2023.07.007.

33. Dong, F.-X., Yan, L., Zhou, X.-H., Huang, S.-T., Liang, J.-Y., Zhang, W.-X., Guo, Z.-W., Guo, P.-R., Qian, W., Kong, L.-J., et al. (2021). Simultaneous adsorption of Cr(VI) and phenol by biochar-based iron oxide composites in water: Performance, kinetics and mechanism. J. Hazard Mater. *416*, 125930. https://doi.org/10.1016/j.jhazmat.2021.125930.

34. Qian, W., Liang, J.-Y., Zhang, W.-X., Huang, S.-T., and Diao, Z.-H. (2022). A porous biochar supported nanoscale zero-valent iron material highly efficient for the simultaneous remediation of cadmium and lead contaminated soil. J. Environ. Sci. *113*, 231–241. https://doi.org/10.1016/j.jes.2021.06.014.

35. Fseha, Y.H., Shaheen, J.F., and Sizirici, B. (2023). Revealing selected groundwater contaminants, risks, and sustainable solutions for safe drinking water through pristine and modified biochar. J. Anal. Appl. Pyrol. *176*, 106237. https://doi.org/10.1016/j.jaap.2023.106237.

36. Ministerio de Agricultura y Ganadería (2023). Panorama Agroestadístico Diciembre 2023. In Boletín Panorama Agroestadístico (SIPA - Sistema de Información Pública Agropecuaria), pp. 1–4. http://sipa.agricultura.gob.ec/index.php/panorama-agroestadistico/2023-panorama-agroestadistico.

37. Lu, F., Rodriguez-Garcia, J., Van Damme, I., Westwood, N.J., Shaw, L., Robinson, J.S., Warren, G., Chatzifragkou, A., McQueen Mason, S., Gomez, L., et al. (2018). Valorisation strategies for cocoa pod husk and its fractions. Curr. Opin. Green Sustainable Chem. *14*, 80–88. https://doi.org/10.1016/j.cogsc.2018.07.007.

38. Marelli, J.-P., Guest, D.I., Bailey, B.A., Evans, H.C., Brown, J.K., Junaid, M., Barreto, R.W., Lisboa, D.O., and Puig, A.S. (2019). Chocolate Under Threat from Old and New Cacao Diseases. Phytopathology *109*, 1331–1343. https://doi.org/10.1094/PHYTO-12-18-0477-RVW.

39. Díaz-Valderrama, J.R., Leiva-Espinoza, S.T., and Aime, M.C. (2020). The History of Cacao and Its Diseases in the Americas. Phytopathology *110*, 1604–1619. https://doi.org/10.1094/PHYTO-05-20-0178-RVW.

40. UN DESA (2023). The Sustainable Development Goals Report 2023: Special Edition. https://unstats.un.org/sdgs/report/2023/.

41. Wang, Q., Wang, Y., Tang, J., Yang, Z., Zhang, L., and Huang, X. (2022). New insights into the interactions between Pb(II) and fruit waste biosorbent. Chemosphere *303*, 135048. https://doi.org/10.1016/j.chemosphere.2022.135048.

42. Zhang, Z., Li, Y., Zong, Y., Yu, J., Ding, H., Kong, Y., Ma, J., and Ding, L. (2022). Efficient removal of cadmium by salts modified-biochar: Performance assessment, theoretical calculation, and quantitative mechanism analysis. Bioresour. Technol. *361*, 127717. https://doi.org/10.1016/j.biortech.2022.127717.

43. Lam, S.S., Liew, R.K., Wong, Y.M., Yek, P.N.Y., Ma, N.L., Lee, C.L., and Chase, H.A. (2017). Microwave-assisted pyrolysis with chemical activation, an innovative method to convert orange peel into activated carbon with improved properties as dye adsorbent. J. Clean. Prod. *162*, 1376–1387. https://doi.org/10.1016/j.jclepro.2017.06.131.

44. Liew, R.K., Nam, W.L., Chong, M.Y., Phang, X.Y., Su, M.H., Yek, P.N.Y., Ma, N.L., Cheng, C.K., Chong, C.T., and Lam, S.S. (2018). Oil palm waste: An abundant and promising feedstock for microwave pyrolysis conversion into good quality biochar with potential multi-applications. Process Saf. Environ. Protect. *115*, 57–69. https://doi.org/10.1016/j.psep.2017.10.005.

45. Vaštyl, M., Jankovská, Z., Cruz, G.J.F., and Matějová, L. (2022). A case study on

microwave pyrolysis of waste tyres and cocoa pod husk; effect on quantity and quality of utilizable products. J. Environ. Chem. Eng. *10*, 106917. https://doi.org/10.1016/j.jece.2021.106917.

46. Ghysels, S., Acosta, N., Estrada, A., Pala, M., De Vrieze, J., Ronsse, F., and Rabaey, K. (2020). Integrating anaerobic digestion and slow pyrolysis improves the product portfolio of a cocoa waste biorefinery. Sustain. Energy Fuels *4*, 3712–3725. https://doi.org/10.1039/D0SE00689K.

47. Zhang, Y., Xu, X., Cao, L., Ok, Y.S., and Cao, X. (2018). Characterization and quantification of electron donating capacity and its structure dependence in biochar derived from three waste biomasses. Chemosphere *211*, 1073–1081. https://doi.org/10.1016/j.chemosphere.2018.08.033.

48. Tsai, W.-T., Hsu, C.-H., Lin, Y.-Q., Tsai, C.-H., Chen, W.-S., and Chang, Y.-T. (2020). Enhancing the Pore Properties and Adsorption Performance of Cocoa Pod Husk (CPH)-Derived Biochars via Post-Acid Treatment. Processes *8*, 144. https://doi.org/10.3390/pr8020144.

49. Wang, Y., Zheng, K., Jiao, Z., Zhan, W., Ge, S., Ning, S., Fang, S., and Ruan, X. (2022). Simultaneous Removal of Cu^{2+}, Cd^{2+} and Pb^{2+} by Modified Wheat Straw Biochar from Aqueous Solution: Preparation, Characterization and Adsorption Mechanism. Toxics *10*, 316. https://doi.org/10.3390/toxics10060316.

50. Nightingale, E.R. (1959). Phenomenological Theory of Ion Solvation. Effective Radii of Hydrated Ions. J. Phys. Chem. *63*, 1381–1387. https://doi.org/10.1021/j150579a011.

51. Volkov, A.G., Paula, S., and Deamer, D.W. (1997). Two mechanisms of permeation of small neutral molecules and hydrated ions across phospholipid bilayers. Bioelectrochem. Bioenerg. *42*, 153–160. https://doi.org/10.1016/S0302-4598(96)05097-0.

52. Rouquerol, J., Avnir, D., Fairbridge, C.W., Everett, D.H., Haynes, J.M., Pernicone, N., Ramsay, J.D.F., Sing, K.S.W., and Unger, K.K. (1994). Recommendations for the characterization of porous solids (Technical Report). Pure Appl. Chem. *66*, 1739–1758. https://doi.org/10.1351/pac199466081739.

53. Ding, W., Dong, X., Ime, I.M., Gao, B., and Ma, L.Q. (2014). Pyrolytic temperatures impact lead sorption mechanisms by bagasse biochars. Chemosphere *105*, 68–74. https://doi.org/10.1016/j.chemosphere.2013.12.042.

54. Rajkovich, S., Enders, A., Hanley, K., Hyland, C., Zimmerman, A.R., and Lehmann, J. (2012). Corn growth and nitrogen nutrition after additions of biochars with varying properties to a temperate soil. Biol. Fertil. Soils *48*, 271–284. https://doi.org/10.1007/s00374-011-0624-7.

55. Smider, B., and Singh, B. (2014). Agronomic performance of a high ash biochar in two contrasting soils. Agric. Ecosyst. Environ. *191*, 99–107. https://doi.org/10.1016/j.agee.2014.01.024.

56. Cantrell, K.B., Hunt, P.G., Uchimiya, M., Novak, J.M., and Ro, K.S. (2012). Impact of pyrolysis temperature and manure source on physicochemical characteristics of biochar. Bioresour. Technol. *107*, 419–428. https://doi.org/10.1016/j.biortech.2011.11.084.

57. Claoston, N., Samsuri, A.W., Ahmad Husni, M.H., and Mohd Amran, M.S. (2014). Effects of pyrolysis temperature on the physicochemical properties of empty fruit bunch and rice husk biochars. Waste Manag. Res. *32*, 331–339. https://doi.org/10.1177/0734242X14525822.

58. Yuan, J.-H., Xu, R.-K., and Zhang, H. (2011). The forms of alkalis in the biochar produced from crop residues at different temperatures. Bioresour. Technol. *102*, 3488–3497. https://doi.org/10.1016/j.biortech.2010.11.018.

59. Albalasmeh, A., Gharaibeh, M.A., Mohawesh, O., Alajlouni, M., Quzaih, M., Masad, M., and El Hanandeh, A. (2020). Characterization and Artificial Neural Networks Modelling of methylene blue adsorption of biochar derived from agricultural residues: Effect of biomass type, pyrolysis temperature, particle size. J. Saudi Chem. Soc. *24*, 811–823. https://doi.org/10.1016/j.jscs.2020.07.005.

60. Krishnamoorthy, N., Nzediegwu, C., Mao, X., Zeng, H., Paramasivan, B., and Chang, S.X. (2023). Biochar seeding properties affect struvite crystallization for soil application. Soil Environ. Health *1*, 100015. https://doi.org/10.1016/j.seh.2023.100015.

61. Ren, H., Cunha, E., Sun, Q., Li, Z., Kinloch, I.A., Young, R.J., and Fan, Z. (2019). Surface functionality analysis by Boehm titration of graphene nanoplatelets functionalized via a solvent-free cycloaddition reaction. Nanoscale Adv. *1*, 1432–1441. https://doi.org/10.1039/C8NA00280K.

62. Schönherr, J., Buchheim, J., Scholz, P., and Adelhelm, P. (2018). Boehm Titration Revisited (Part I): Practical Aspects for Achieving a High Precision in Quantifying Oxygen-Containing Surface Groups on Carbon Materials. J. Carbon Res. *4*, 21. https://doi.org/10.3390/c4020021.

63. Fahmi, A.H., Samsuri, A.W., Jol, H., and Singh, D. (2018). Physical modification of biochar to expose the inner pores and their functional groups to enhance lead adsorption. RSC Adv. *8*, 38270–38280. https://doi.org/10.1039/C8RA06867D.

64. Eletta, O.A.A., Adeniyi, A.G., Ighalo, J.O., Onifade, D.V., and Ayandele, F.O. (2020). Valorisation of Cocoa (Theobroma cacao) pod husk as precursors for the production of adsorbents for water treatment. Environ. Technol. Rev. *9*, 20–36. https://doi.org/10.1080/21622515.2020.1730983.

65. Akinjokun, A.I., Petrik, L.F., Ogunfowokan, A.O., Ajao, J., and Ojumu, T.V. (2021). Isolation and characterization of nanocrystalline cellulose from cocoa pod husk (CPH) biomass wastes. Heliyon *7*, e06680. https://doi.org/10.1016/j.heliyon.2021.e06680.

66. Olu-Owolabi, B., Oputu, O., Adebowale, K.O., Ogunsolu, T., and Olujimi, O. (2012). Biosorption of Cd^{2+} and Pb^{2+} ions onto mango stone and cocoa pod waste: Kinetic and equilibrium studies. Sci. Res. Essays *7*, 1614–1629. https://doi.org/10.5897/SRE11.2248.

67. Chowdhury, Z.Z., Zain, S.M., Khan, R.A., and Islam, M.S. (2012). Preparation and characterizations of activated carbon from kenaf fiber for equilibrium adsorption studies of copper from wastewater. Korean J. Chem. Eng. *29*, 1187–1195. https://doi.org/10.1007/s11814-011-0297-9.

68. Baccile, N., Falco, C., and Titirici, M.-M. (2014). Characterization of biomass and its derived char using ^{13}C-solid state nuclear magnetic resonance. Green Chem. *16*, 4839–4869. https://doi.org/10.1039/C3GC42570C.

69. Smernik, R.J. (2017). Analysis of biochars by ^{13}C nuclear magnetic resonance spectroscopy. In Biochar: a guide to analytical methods, B. Singh, M. Camps-Arbestain, and J. Lehmann, eds. (CSIRO Publishing and CRC Press/Taylor and Francis Group, LLC), pp. 151–161. www.crcpress.com.

70. Sumaraj, Xiong, Z., Xiong, Z., Sarmah, A.K., and Padhye, L.P. (2020). Acidic surface functional groups control chemisorption of ammonium onto carbon materials in aqueous media. Sci. Total Environ. *698*, 134193. https://doi.org/10.1016/j.scitotenv.2019.134193.

71. Bourauel, C., Fries, T., Drescher, D., and Plietsch, R. (1998). Surface roughness of orthodontic wires via atomic force microscopy, laser specular reflectance, and profilometry. Eur. J. Orthod. *20*, 79–92. https://doi.org/10.1093/ejo/20.1.79.

72. Huang, S., Du, P., Min, C., Liao, Y., Sun, H., and Jiang, Y. (2013). Poly(1-amino-5-chloroanthraquinone): Highly Selective and Ultrasensitive Fluorescent Chemosensor For Ferric Ion. J. Fluoresc. *23*, 621–627. https://doi.org/10.1007/s10895-013-1179-9.

73. Ramón de los Santos, C., Barajas Fernández, J., Pérez Hernández, G., Hernández Rivera, M.Á., and Díaz Flores, L.L. (2019). Adsorción de cobre (II) y cadmio (II) en suspensiones acuosas de $CaCO_3$ biogénico nanoestructurado. Bol. Soc. Espanola Ceram. Vidr. *58*, 2–13. https://doi.org/10.1016/j.bsecv.2018.05.003.

74. Wu, F., Chen, L., Hu, P., Zhou, X., Zhou, H., Wang, D., Lu, X., and Mi, B. (2022). Comparison of properties, adsorption performance and mechanisms to Cd(II) on lignin-derived biochars under different pyrolysis temperatures by microwave heating. Environ. Technol. Innov. *25*, 102196. https://doi.org/10.1016/j.eti.2021.102196.

75. Rahmani, A., Mousavi, H.Z., and Fazli, M. (2010). Effect of nanostructure alumina on adsorption of heavy metals. Desalination *253*, 94–100. https://doi.org/10.1016/j.desal.2009.11.027.

76. Brickler, C.A., Wu, Y., Li, S., Anandhi, A., and Chen, G. (2021). Comparing Physicochemical Properties and Sorption Behaviors of Pyrolysis-Derived and Microwave-Mediated Biochar. Sustainability *13*, 2359. https://doi.org/10.3390/su13042359.

77. Pinzon-Nuñez, D.A., Adarme-Duran, C.A., Vargas-Fiallo, L., Rodriguez-Lopez, N., and Rios-Reyes, C.A. (2022). Biochar as a waste management strategy for cadmium contaminated cocoa pod husk residues. Int. J. Recycl. Org. Waste Agric. *11*, 101–115. https://doi.org/10.30486/ijrowa.2021.1920124.1192.

78. Abbey, C.Y.B., Duwiejuah, A.B., and Quianoo, A.K. (2023). Removal of toxic metals from aqueous phase using cacao pod husk biochar in the era of green chemistry. Appl. Water Sci. *13*, 57. https://doi.org/10.1007/s13201-022-01863-5.

79. Aderonke, A.O., Abimbola, B.A., Ifeanyi, E., Omotayo, S.A., Oluwagbemiga, S.A., and Oladotun, W.M. (2014). Adsorption of heavy metal ions onto chitosan grafted cocoa husk char. Afr. J. Pure Appl. Chem. *8*, 147–161. https://doi.org/10.5897/AJPAC2014.0591.

80. Odubiyi, O.A., Awoyale, A.A., and Eloka-Eboka, A.C. (2012). Wastewater Treatment with Activated Charcoal Produced from Cocoa Pod Husk. Int. J. Environ. Bioenergy 4, 162–175. https://modernscientificpress.com/Journals/ViewArticle.aspx?gkN1Z6Pb60HNQPymfPQIZOvOz7KgjeU4y3KCzHbx2RQAfsHh/ocdhgKpygnEAdob.

81. Osakwe, C., Sanni, I., Sa'id, S., and Zubairu, A. (2014). Adsorption of Heavy Metals from Wastewaters Using Adonosia digitata Fruit Shells and Theobroma cacao Pods as Adsorbents: A Comparative Study. AU J. Technol. 18, 11–18. http://www.assumptionjournal.au.edu/index.php/aujournaltechnology/article/view/1212/1068.

82. Tran, H.N., You, S.-J., Hosseini-Bandegharaei, A., and Chao, H.-P. (2017). Mistakes and inconsistencies regarding adsorption of contaminants from aqueous solutions: A critical review. Water Res. 120, 88–116. https://doi.org/10.1016/j.watres.2017.04.014.

83. Machrafi, H. (2022). Surface tension of nanoparticle dispersions unravelled by size-dependent non-occupied sites free energy versus adsorption kinetics. NPJ Microgravity 8, 47. https://doi.org/10.1038/s41526-022-00234-3.

84. Mechi, N., Ben Khemis, I., Dotto, G.L., Franco, D., Sellaoui, L., and Ben Lamine, A. (2019). Investigation of the adsorption mechanism of methylene blue (MB) on Cortaderia selloana flower spikes (FSs) and on Cortaderia selloana flower spikes derived carbon fibers (CFs). J. Mol. Liq. 280, 268–273. https://doi.org/10.1016/j.molliq.2019.02.024.

85. Cheng, S., Zhang, L., Xia, H., Peng, J., Shu, J., Li, C., Jiang, X., and Zhang, Q. (2017). Adsorption behavior of methylene blue onto waste-derived adsorbent and exhaust gases recycling. RSC Adv. 7, 27331–27341. https://doi.org/10.1039/C7RA01482A.

86. Yao, Y., Xu, F., Chen, M., Xu, Z., and Zhu, Z. (2010). Adsorption behavior of methylene blue on carbon nanotubes. Bioresour. Technol. 101, 3040–3046. https://doi.org/10.1016/j.biortech.2009.12.042.

87. Shikuku, V.O., Zanella, R., Kowenje, C.O., Donato, F.F., Bandeira, N.M.G., and Prestes, O.D. (2018). Single and binary adsorption of sulfonamide antibiotics onto iron-modified clay: linear and nonlinear isotherms, kinetics, thermodynamics, and mechanistic studies. Appl. Water Sci. 8, 175. https://doi.org/10.1007/s13201-018-0825-4.

88. Zambrano-Intriago, L., Gorozabel, M., Mosquera, A., Delgado-Demera, H., Duarte, M., and Rodríguez-Díaz, J. (2022). Kinetics, equilibrium, and thermodynamics of the blue 19 dye adsorption process using residual biomass attained from rice cultivation. Biomass Convers. Biorefin. 12, 3843–3855. https://doi.org/10.1007/s13399-020-00944-2.

89. Forgionny, A., Acelas, N.Y., Jimenez-Orozco, C., and Flórez, E. (2020). Toward the design of efficient adsorbents for Hg^{2+} removal: Molecular and thermodynamic insights. Int. J. Quant. Chem. 120, e26258. https://doi.org/10.1002/qua.26258.

90. Qin, H., He, P., Wu, J., and Chen, N. (2020). Theoretical study of hydrocarbon functional groups on elemental mercury adsorption on carbonaceous surface. Chem. Eng. J. 380, 122505. https://doi.org/10.1016/j.cej.2019.122505.

91. Xie, N., Wang, H., and You, C. (2021). Role of oxygen functional groups in Pb^{2+} adsorption from aqueous solution on carbonaceous surface: A density functional theory study. J. Hazard Mater. 405, 124221. https://doi.org/10.1016/j.jhazmat.2020.124221.

92. Fang, L., Li, Z., Wu, C., Jiao, S., Gao, Z., Gates, I.D., Ding, X., and Yang, W. (2023). Understanding adsorption mechanisms of mercury over unburned carbon. Fuel 333, 126399. https://doi.org/10.1016/j.fuel.2022.126399.

93. Chen, N., and Yang, R.T. (1998). Ab Initio Molecular Orbital Study of the Unified Mechanism and Pathways for Gas−Carbon Reactions. J. Phys. Chem. A 102, 6348–6356. https://doi.org/10.1021/jp981518g.

94. Bruno, I.J., Cole, J.C., Edgington, P.R., Kessler, M., Macrae, C.F., McCabe, P., Pearson, J., and Taylor, R. (2002). New software for searching the Cambridge Structural Database and visualizing crystal structures. Acta Crystallogr. B 58, 389–397. https://doi.org/10.1107/S0108768102003324.

95. Yoro, K.O., Amosa, M.K., Sekoai, P.T., Mulopo, J., and Daramola, M.O. (2020). Diffusion mechanism and effect of mass transfer limitation during the adsorption of CO_2 by polyaspartamide in a packed-bed unit. Int. J. Sustain. Eng. 13, 54–67. https://doi.org/10.1080/19397038.2019.1592261.

96. Wang, J., and Guo, X. (2020). Adsorption kinetic models: Physical meanings, applications, and solving methods. J. Hazard Mater. 390, 122156. https://doi.org/10.1016/j.jhazmat.2020.122156.

97. Borsari, M. (2014). Cadmium: Coordination Chemistry. In Encyclopedia of Inorganic and Bioinorganic Chemistry (Wiley), pp. 1–16. https://doi.org/10.1002/9781119951438.eibc2261.

98. Fodah, A.E.M., and Abdelwahab, T.A.M. (2022). Process optimization and technoeconomic environmental assessment of biofuel produced by solar powered microwave pyrolysis. Sci. Rep. 12, 12572. https://doi.org/10.1038/s41598-022-16171-w.

99. García, R., Pizarro, C., Lavín, A.G., and Bueno, J.L. (2013). Biomass proximate analysis using thermogravimetry. Bioresour. Technol. 139, 1–4. https://doi.org/10.1016/j.biortech.2013.03.197.

100. Rodríguez-Díaz, J., García, J., Sánchez, L., Silva, M., Silva, V., and Arteaga-Pérez, L. (2015). Comprehensive Characterization of Sugarcane Bagasse Ash for Its Use as an Adsorbent. BioEnergy Res. 8, 1885–1895. https://doi.org/10.1007/s12155-015-9646-6.

101. Gurvitsch, L.G. (1915). Physicochemical attractive force. J. Russ. Phys. Chem. Soc. 47, 805–827.

102. Cristiano, E., Hu, Y.-J., Sigfried, M., Kaplan, D., and Nitsche, H. (2011). A Comparison of Point of Zero Charge Measurement Methodology. Clays Clay Miner. 59, 107–115. https://doi.org/10.1346/CCMN.2011.0590201.

103. Hendershot, W.H., and Duquette, M. (1986). A Simple Barium Chloride Method for Determining Cation Exchange Capacity and Exchangeable Cations. Soil Sci. Soc. Am. J. 50, 605–608. https://doi.org/10.2136/sssaj1986.03615995005000030013x.

104. Goertzen, S.L., Thériault, K.D., Oickle, A.M., Tarasuk, A.C., and Andreas, H.A. (2010). Standardization of the Boehm titration. Part I. CO_2 expulsion and endpoint determination. Carbon 48, 1252–1261. https://doi.org/10.1016/j.carbon.2009.11.050.

105. Li, X., Shen, Q., Zhang, D., Mei, X., Ran, W., Xu, Y., and Yu, G. (2013). Functional Groups Determine Biochar Properties (pH and EC) as Studied by Two-Dimensional ^{13}C NMR Correlation Spectroscopy. PLoS One 8, e65949. https://doi.org/10.1371/journal.pone.0065949.

106. Gates-Rector, S., and Blanton, T. (2019). The Powder Diffraction File: a quality materials characterization database. Powder Diffr. 34, 352–360. https://doi.org/10.1017/S0885715619000812.

107. Su, D., Wang, M., Xu, H., Zhang, Y., Hu, Q., Ren, Y., and He, J. (2023). Performance and mechanism of Ficus carica branch waste based biochar in removing Cd^{2+} from aqueous solution. Biomass Convers. Biorefin. 1–4. https://doi.org/10.1007/s13399-023-04690-z.

108. Chimera. A tool for extracting PhreeqC databases into SPANA formatAmphos 21. https://www.amphos21.com/.

109. Ortega Navarro, E., Martí Calatayud, M.C., Pérez Herranz, V., García Gabaldón, M., and Carrillo Abad, J. (2020). Uso combinado de software libre y de técnicas analíticas para facilitar la comprensión de los diagramas de equilibrio químico. Rev. Interuniv. Invest. Tecnol. Educ. 8, 1–16. https://doi.org/10.6018/riite.391411.

110. Wang, J., and Guo, X. (2022). Rethinking of the intraparticle diffusion adsorption kinetics model: Interpretation, solving methods and applications. Chemosphere 309, 136732. https://doi.org/10.1016/j.chemosphere.2022.136732.

111. Weber, W.J. (1984). Evolution of a Technology. J. Environ. Eng. 110, 899–917. https://doi.org/10.1061/(ASCE)0733-9372(1984)110:5(899.

112. Boyd, G.E., Adamson, A.W., and Myers, L.S. (1947). The Exchange Adsorption of Ions from Aqueous Solutions by Organic Zeolites. II. Kinetics 1. J. Am. Chem. Soc. 69, 2836–2848. https://doi.org/10.1021/ja01203a066.

113. Reichenberg, D. (1953). Properties of Ion-Exchange Resins in Relation to their Structure. III. Kinetics of Exchange. J. Am. Chem. Soc. 75, 589–597. https://doi.org/10.1021/ja01099a022.

114. Singh, P.K., Banerjee, S., Srivastava, A.L., and Sharma, Y.C. (2015). Kinetic and equilibrium modeling for removal of nitrate from aqueous solutions and drinking water by a potential adsorbent, hydrous bismuth oxide. RSC Adv. 5, 35365–35376. https://doi.org/10.1039/C4RA11213J.

115. Weber, W.J., and Morris, J.C. (1963). Kinetics of Adsorption on Carbon from Solution. J. Sanit. Eng. Div. 89, 31–59. https://doi.org/10.1061/JSEDAI.0000430.

116. McKay, G. (1980). The removal of colour from effluent using various adsorbents—III. Silica: Rate processes. Water Res. 14, 15–20. https://doi.org/10.1016/0043-1354(80)90037-8.

117. Ritchie, A.G. (1977). Alternative to the Elovich equation for the kinetics of adsorption of gases on solids. J. Chem. Soc., Faraday Trans. 1 73, 1650. https://doi.org/10.1039/f19777301650.

118. Lagergren, S. (1898). About the theory of so-called adsorption of soluble substances. K. Sven. Vetenskapsakad. Handl. 24, 1–39.

119. Plazinski, W., Rudzinski, W., and Plazinska, A. (2009). Theoretical models of sorption kinetics including a surface reaction mechanism: A review. Adv. Colloid Interface Sci. *152*, 2–13. https://doi.org/10.1016/j.cis.2009.07.009.

120. Blanchard, G., Maunaye, M., and Martin, G. (1984). Removal of heavy metals from waters by means of natural zeolites. Water Res. *18*, 1501–1507. https://doi.org/10.1016/0043-1354(84)90124-6.

121. Azizian, S. (2004). Kinetic models of sorption: a theoretical analysis. J. Colloid Interface Sci. *276*, 47–52. https://doi.org/10.1016/j.jcis.2004.03.048.

122. Guo, X., and Wang, J. (2019). A general kinetic model for adsorption: Theoretical analysis and modeling. J. Mol. Liq. *288*, 111100. https://doi.org/10.1016/j.molliq.2019.111100.

123. Roginsky, S., and Zeldovich, Y.B. (1934). The catalytic oxidation of carbon monoxide on manganese dioxide. Acta Phys. Chem. USSR *1*, 2019.

124. Teng, H., and Hsieh, C.-T. (1999). Activation Energy for Oxygen Chemisorption on Carbon at Low Temperatures. Ind. Eng. Chem. Res. *38*, 292–297. https://doi.org/10.1021/ie980107j.

125. Kumar, K.V., and Sivanesan, S. (2005). Comparison of linear and non-linear method in estimating the sorption isotherm parameters for safranin onto activated carbon. J. Hazard Mater. *123*, 288–292. https://doi.org/10.1016/j.jhazmat.2005.03.040.

126. Ho, Y.-S. (2006). Second-order kinetic model for the sorption of cadmium onto tree fern: A comparison of linear and non-linear methods. Water Res. *40*, 119–125. https://doi.org/10.1016/j.watres.2005.10.040.

127. Kumar, K.V., Porkodi, K., and Rocha, F. (2008). Comparison of various error functions in predicting the optimum isotherm by linear and non-linear regression analysis for the sorption of basic red 9 by activated carbon. J. Hazard Mater. *150*, 158–165. https://doi.org/10.1016/j.jhazmat.2007.09.020.

128. Langmuir, I. (1918). The adsorption of gases on plane surfaces of glass, mica and platinum. J. Am. Chem. Soc. *40*, 1361–1403. https://doi.org/10.1021/ja02242a004.

129. Freundlich, H. (1907). Über die Adsorption in Lösungen. Z. Phys. Chem. *57U*, 385–470. https://doi.org/10.1515/zpch-1907-5723.

130. Redlich, O., and Peterson, D.L. (1959). A Useful Adsorption Isotherm. J. Phys. Chem. *63*, 1024. https://doi.org/10.1021/j150576a611.

131. Wu, F.-C., Liu, B.-L., Wu, K.-T., and Tseng, R.-L. (2010). A new linear form analysis of Redlich–Peterson isotherm equation for the adsorptions of dyes. Chem. Eng. J. *162*, 21–27. https://doi.org/10.1016/j.cej.2010.03.006.

132. Bolster, C.H., and Hornberger, G.M. (2007). On the Use of Linearized Langmuir Equations. Soil Sci. Soc. Am. J. *71*, 1796–1806. https://doi.org/10.2136/sssaj2006.0304.

133. Worch, E. (2012). Adsorption Technology in Water Treatment (DE GRUYTER). https://doi.org/10.1515/9783110240238.

134. Ho, Y.-S. (2004). Selection of optimum sorption isotherm. Carbon *42*, 2115–2116. https://doi.org/10.1016/j.carbon.2004.03.019.

135. Osmari, T.A., Gallon, R., Schwaab, M., Barbosa-Coutinho, E., Severo, J.B., and Pinto, J.C. (2013). Statistical Analysis of Linear and Nonlinear Regression for the Estimation of Adsorption Isotherm Parameters. Adsorpt. Sci. Technol. *31*, 433–458. https://doi.org/10.1260/0263-6174.31.5.433.

136. Shahmohammadi-Kalalagh, S., and Babazadeh, H. (2014). Isotherms for the sorption of zinc and copper onto kaolinite: comparison of various error functions. Int. J. Environ. Sci. Technol. *11*, 111–118. https://doi.org/10.1007/s13762-013-0260-x.

137. González-López, M.E., Laureano-Anzaldo, C.M., Pérez-Fonseca, A.A., Arellano, M., and Robledo-Ortíz, J.R. (2022). A Critical Overview of Adsorption Models Linearization: Methodological and Statistical Inconsistencies. Separ. Purif. Rev. *51*, 358–372. https://doi.org/10.1080/15422119.2021.1951757.

138. Hall, K.R., Eagleton, L.C., Acrivos, A., and Vermeulen, T. (1966). Pore- and Solid-Diffusion Kinetics in Fixed-Bed Adsorption under Constant-Pattern Conditions. Ind. Eng. Chem. Fund. *5*, 212–223. https://doi.org/10.1021/i160018a011.

139. Weber, T.W., and Chakravorti, R.K. (1974). Pore and solid diffusion models for fixed-bed adsorbers. AIChE J. *20*, 228–238. https://doi.org/10.1002/aic.690200204.

140. Zhou, X., and Zhou, X. (2014). The unit problem in the thermodynamic calculation of adsorption using the Langmuir equation. Chem. Eng. Commun. *201*, 1459–1467. https://doi.org/10.1080/00986445.2013.818541.

141. Frisch, M.J., Trucks, G.W., Schlegel, H.B., Scuseria, G.E., Robb, M.A., Cheeseman, J.R., Scalmani, G., Barone, V., Petersson, G.A., Nakatsuji, H., et al. (2016). Gaussian 16 Rev. C.01.

142. Ghazi, Z.A., Khattak, A.M., Iqbal, R., Ahmad, R., Khan, A.A., Usman, M., Nawaz, F., Ali, W., Felegari, Z., Jan, S.U., et al. (2018). Adsorptive removal of Cd^{2+} from aqueous solutions by a highly stable covalent triazine-based framework. New J. Chem. *42*, 10234–10242. https://doi.org/10.1039/C8NJ01778F.

143. Hussain, M., Khaliq, N., Nisar, A., Khan, M., Karim, S., Ali Khan, A., Yi, X., Maqbool, M., and Ali, G. (2020). TiO_2 nanotube array-modified electrodes for L-cysteine biosensing: Experimental and density-functional theory study. Nanotechnology *31*, 505501. https://doi.org/10.1088/1361-6528/abb431.

144. Schaftenaar, G., Vlieg, E., and Vriend, G. (2017). Molden 2.0: quantum chemistry meets proteins. J. Comput. Aided Mol. Des. *31*, 789–800. https://doi.org/10.1007/s10822-017-0042-5.

145. Schaftenaar, G., and Noordik, J.H. (2000). Molden: a pre- and post-processing program for molecular and electronic structures. J. Comput. Aided Mol. Des. *14*, 123–134. https://doi.org/10.1023/a:1008193805436.

146. Grimme, S., Ehrlich, S., and Goerigk, L. (2011). Effect of the damping function in dispersion corrected density functional theory. J. Comput. Chem. *32*, 1456–1465. https://doi.org/10.1002/jcc.21759.

147. Becke, A.D., and Johnson, E.R. (2005). A density-functional model of the dispersion interaction. J. Chem. Phys. *123*, 154101. https://doi.org/10.1063/1.2065267.

148. Becke, A.D., and Johnson, E.R. (2006). Exchange-hole dipole moment and the dispersion interaction: High-order dispersion coefficients. J. Chem. Phys. *124*, 14104. https://doi.org/10.1063/1.2139668.

149. Zhao, N., Zhao, C., Liu, K., Zhang, W., Tsang, D.C.W., Yang, Z., Yang, X., Yan, B., Morel, J.L., and Qiu, R. (2021). Experimental and DFT investigation on N-functionalized biochars for enhanced removal of Cr(VI). Environ. Pollut. *291*, 118244. https://doi.org/10.1016/j.envpol.2021.118244.

150. Weigend, F., and Ahlrichs, R. (2005). Balanced basis sets of split valence, triple zeta valence and quadruple zeta valence quality for H to Rn: Design and assessment of accuracy. Phys. Chem. Chem. Phys. *7*, 3297–3305. https://doi.org/10.1039/B508541A.

151. Weigend, F. (2006). Accurate Coulomb-fitting basis sets for H to Rn. Phys. Chem. Chem. Phys. *8*, 1057–1065. https://doi.org/10.1039/B515623H.

152. Lipparini, F., Scalmani, G., Mennucci, B., Cancès, E., Caricato, M., and Frisch, M.J. (2010). A variational formulation of the polarizable continuum model. J. Chem. Phys. *133*, 014106. https://doi.org/10.1063/1.3454683.

153. OriginLab Corporation (2023). Origin(Pro), Version 2023 (OriginLab Corporation (Northampton, MA)).

STAR★METHODS

KEY RESOURCES TABLE

REAGENT or RESOURCE	SOURCE	IDENTIFIER
Chemicals, peptides, and recombinant proteins		
Sodium hydroxide (NaOH) 99.9 %	Merck	CAS: 12179-02-1
Hydrochloric acid (HCl) 37 %	Merck	CAS: 7647-01-0
Nitric acid (HNO$_3$) 68 %	Fisher Scientific	CAS: 7697-37-2
Cadmium nitrate Cd(NO$_3$)$_2$·4H$_2$O	Sigma–Aldrich	CAS: 10022-68-1
Cadmium AA standard (1,000 mg/L in 2-5% Nitric Acid)	AccuStandard	CAS: 7440-43-9
Ultrapure water (Reagent water)	Prepared in laboratory	ASTM type I water
Acetylene gas grade 2.5 AA	Linde	https://www.lindedirect.com
Software and algorithms		
Origin 2023	Origin Lab	https://www.originlab.com/2023
Excel	Microsoft 365	https://www.microsoft.com/es-ec/
Chimera (Spana Format)	Chimera	https://techlabs.amphos21.com/technology/chimera/
PDF-5+ database	ICDD (International Centre for Diffraction Data)	https://www.icdd.com/
FAIRE	CCDC (Cambridge Crystallographic Data Centre)	https://www.ccdc.cam.ac.uk/community/ccdc-for-the-community/faire-grants/
Gaussian 16 software package	Gaussian, Inc.	https://gaussian.com/dft/
MOLDEN, processing program of molecular and electronic structure	Institute for Molecules and Materials, Radboud University Nijmegen	https://www.theochem.ru.nl/molden/
Other		
Thermogravimetric analysis (TGA) STAR system	Metter Toledo – Germany	https://www.mt.com/us/en/home/products/Laboratory_Analytics_Browse/TA_Family_Browse/TGA.html
vario MACRO cube organic elemental analyzer	Elementar – Germany	https://www.elementar.com/en/products/organic-elemental-analyzers/vario-macro-cube
AutoChem II 2920 automated catalyst characterization system	Micromeritics – USA	https://www.micromeritics.com/micromeritics-autochem-ii-2920-automated-catalyst-characterization-system/
Nanopartica SZ-100 series nanoparticle analyzer	Horiba Scientific – Japan	https://www.horiba.com/int/scientific/products/detail/action/show/Product/sz-100-1356/
Spectrum Two FTIR spectrometer	PerkinElmer Inc. – USA	https://www.perkinelmer.com/product/spectrum-two-ft-ir-sp10-software-l160000a
Solid State Nuclear Magnetic Resonance (ssNMR) – Avance III spectrometer	Bruker – Germany	https://www.bruker.com
Scanning Electron Microscopy (SEM)/Energy Dispersive X-ray spectroscopy (EDX) – VEGA II microscope	Tescan – USA	https://www.tescan.com/
Atomic Force Microscopy (AFM) – NX10 microscope	Park Systems	https://www.parksystems.com/17-products/park-nx10
X-Ray Powder Diffraction (XRPD) – D2 phaser diffractometer	Bruker – Germany	https://www.bruker.com/
YR55 water purifying system	Kalstein – France	https://kalstein.net/en/water-purification-systems/

Continued

REAGENT or RESOURCE	SOURCE	IDENTIFIER
Flame Atomic Absorption Spectrometry (FAAS) – AAnalyst 400 spectrophotometer	PerkinElmer Inc. – USA	https://resources.perkinelmer.com/lab-solutions/resources/docs/BRO_AAnalyst-200-400.pdf
Cutting mill (SM300)	Retsch GmbH	https://www.retsch.com/products/milling/cutting-mills/
Infrared camera (Ti450)	Fluke Corporation	https://www.fluke.com/en-us/product/thermal-cameras/ti450
Domestic microwave oven (Microwave LG MS1536GIR) with "Inverter Technology"	LG Electronics	https://www.lg.com/ec/microondas/lg-MS1536GIR

RESOURCE AVAILABILITY

Lead contact

Further information and requests for resources should be directed to the lead contact, Prof. Yonathan J. Parra (molemater@uce.edu.ec).

Materials availability

This study did not generate new unique reagents.

Data and code availability

- All data reported in this paper will be shared by the lead contact upon request.
- This study did not generate original code.
- Any additional information required to reanalyze the data reported in this paper is available from the lead contact upon reasonable request.

EXPERIMENTAL MODEL AND STUDY PARTICIPANT DETAILS

Our study does not use any experimental models.

METHOD DETAILS

CPH biomass preparation

The CPH biomass was collected from cocoa plantations in the Convento parish in the Chone canton of the Manabí province, Ecuador. The pretreatment of the CPH was initiated by washing the feedstock with abundant distilled water to eliminate impurities that could interfere in the processing of the raw material. The CPHs were then allowed to dry for seven days at ambient temperature in a well-ventilated area. The dried CPHs were manually crushed in a mortar and the particle size was reduced in a cutting mill (Retsch, SM300) using a 4.0 mm bottom sieve. Furthermore, the material was classified using mesh #5 and #18 sieves to separate the dust fraction, retaining a particle size between 4.00 and 1.00 mm. The milled and sieved CPHs were collected and stored in Ziploc® bags.

Biochar preparation by MAP

100 g of dried, milled and sieved CPH were placed in a quartz glass container (inner diameter: 65 mm; height: 87 mm), covered with a quartz lid to prevent atmospheric oxygen from entering, but allowing the generated gases to escape. For the MAP experiments, a domestic microwave oven (Microwave LG MS1536GIR) with "Inverter Technology" was used, allowing a stable microwave irradiation power with selectable intensity. The chosen output power was 720 W, and the reaction time was held constant at 15 minutes, reaching a temperature of approximately 730 K, which was measured with an infrared camera (Fluke Ti450).[98] The yield of the resulting BCCPH was calculated using Equation 6.

$$\text{Yield (wt\%)} = \frac{W_f}{W_i} \times 100 \qquad \text{(Equation 6)}$$

W_f is the weight of BCCPH and W_i is the weight of CPH, both in grams. The BCCPH was then sieved using mesh #8 and #10 (particle sizes between 2.38 to 2.00 mm) and stored inside a sample vial, ready for analysis. The MAP experiments were repeated three times to ensure good data reproducibility. The criteria for selecting biochar particle size was to enhance filtration efficiency and reduce solution turbidity, counteracting the agglomeration issues and analytical inaccuracies associated with smaller particles.

Characterization of feedstock and biochar

The prepared CPH and BCCPH were characterized using various analyses. Proximal analyses were carried out using a thermogravimetric analyzer (TGA) (Mettler Toledo, TGA1), determining moisture, volatile matter, fixed carbon, and ashes in a single experiment,[99] achieving similar results to those obtained by the respective ASTM methods. TGA runs were carried out, applying the following temperature profile: starting at 298 K in an N_2 atmosphere (20 mL/min), with a temperature ramp of 283 K/min until reaching 373 K, maintaining this plateau for 15 min (for moisture determination), followed by a temperature ramp of 283 K/min, until reaching 973 K (for volatile matter and fixed carbon determination). Then, the atmosphere was switched from nitrogen to synthetic air (50 mL/min), maintaining this plateau for 30 min (for ash determination). The analyses were conducted at 540 mmHg (atmospheric pressure in Quito, Ecuador). The C, H, N and S elements of the CPH and BCCPH were determined using an elemental analyzer (vario MACRO cube, Elementar, Germany) using helium as a carrier gas. The oxygen content was calculated by difference [100 - (C + H + N + S)]. For the BET-specific surface area (SSA) and total pore volume (TPV) (Micromeritics, Autochem II 2920), approximately 0.8 g of sample material was degassed at 373 K for 2 h. Afterwards, the parameters were determined based on the adsorption / desorption of N_2.[100] Pore diameter (D) was calculated using the Gurvitsch rule (D = 4TPV/SSA).[101] It assumes homogeneity in diameter, cylindrical and rigid pores. To measure the pH of CPH and BCCPH suspensions, the protocol of the ASTM D 1512 – 15b (2020) standard was followed.[54] Electric conductivity (EC) was also measured for BCCPH. The pH value at the point of zero charge (pH$_{PZC}$) of the BCCPH was determined by the following procedure:[102] a stock solution of 0.1 M KCl was prepared (1 L) and 50 mL of this solution were added into each of six different beakers. In each beaker, the pH of the solution was adjusted by adding 0.1 M NaOH or 0.1 M HCl to obtain an initial pH (pH$_i$) from 2 to 12 in increments of 2. Finally, 50 mL of each solution were transferred to an Erlenmeyer flask and 0.1 g of BCCPH was added to each flask. The suspensions in the flasks were stirred at 300 revolutions per minute (rpm) for 4 h and the final pH value (pH$_f$) of the supernatant liquid was recorded. The difference between pH$_f$ and pH$_i$ (ΔpH = pH$_f$ − pH$_i$) was plotted against pH$_i$, and the point of the intersection of the resulting curve and ΔpH$_i$ determined the PZC (Figure S1). All pH and EC measurements were carried out using a multiparameter bench meter (Milwaukee, Mi 180 Bench Meter). The cation exchange capacity (CEC) of the biomass and the biochar were determined according to the procedure described in the literature.[103] To measure the Zeta potential (ZP), 0.1 g of BCCPH (0.063 mm, mesh #230) was weighed into a beaker of 100 mL, 50 mL deionized water was added, and the samples were stirred for 24 h until a suspension was obtained. Afterwards, 12 μL of the suspension was put in a measurement cell to be examined (Figure S2) with a Horiba Nanoparticle analyzer SZ-100.[60] The concentration and type of functional groups of the BCCPH's surface were determined by applying the Boehm titration method according to the procedure described in the literature (Tables S1 and S2).[61,104] The functional groups on the CPH and BCCPH surface were characterized through a Fourier transform infrared spectroscopy (FTIR) analysis using a PerkinElmer Spectrum Two spectrometer with an optical system of potassium bromide (KBr) windows to collect data in the range of 4,000-400 cm^{-1}. The functional groups on the BCCPH and BCCPH-Cd surface also were characterized through Solid State Nuclear Magnetic Resonance (ssNMR) in a 400 MHz Bruker Avance III (9.4 T); the samples were packed in 4 mm zirconia rotors and the spectra were recorded by spinning at 10 kHz under Magic Angle Spinning (MAS) conditions at 298 K using Cross Polarization (CP) with D1 of 1s, p15 of 3,500 μs, around 64 K scans (NS), 1,000 μs contact time. The ssNMR spectroscopy is only a qualitative rather than quantitative method.[105] The morphology and superficial element composition of BCCPH were examined using scanning electron microscopy (SEM) at 10 kV and energy dispersive X-ray spectroscopy (EDS / EDX, Table S3; Figures S3 and S4), (TESCAN VEGA II), respectively. Micro and nanotopographic analyses of BCCPH were carried out using the Park System NX10 atomic force microscope (AFM) in non-contact mode. The topography was evaluated through the van der Waals forces between the sample surface and the Point Probe Plus silicon sensor tip (PPP-NCLR). Biochar tablets were created and placed in the sample holder using double-sided tape for further analysis. A scan speed of 0.5 Hz, a 10 nm setpoint and a 2.5 × 2.5 μm scan area were used. The X-ray Powder Diffraction (XRPD) pattern of the BCCPH was recorded on a Bruker D2 Phaser X-ray diffractometer using a Co (1.78896 Å) radiation source, operating at 30 kV and 10 mA. The patterns were registered from 4° to 90° in 2Θ in steps of 0.02°, at scan speeds (time / step) of 18.00 s, in 4,300 steps for a total time of 77,400 s. A divergence slit (0.6 mm) was used. Samples were mounted on a zero-background sample holder and rotated at 15 rpm. The X-ray Powder Diffraction (XRPD) pattern of the BCCPH-Cd was recorded on a PANalytical Empyrean X-ray diffractometer using a Cu (1.54056 Å) radiation source, operating at 40 kV and 30 mA. The patterns were registered from 4° to 90° in 2Θ in steps of 0.02°, at scan speeds (time / step) of 15.00 s, in 4,300 steps for a total time of 64,500 s. A divergence slit (1°) and incident beam mask (15 mm) were used. The analyses of the X-ray powder diffraction patterns were carried out using the Sleve+ facility of ICDD's PDF-5+ database.[106]

Adsorption experiments

Cd(NO$_3$)$_2$·4H$_2$O was used to prepare the stock solution (300 mg/L) in deionized water. All the experiments were done by diluting the stock solution until the desired concentration was attained.[107]

Adsorption experiments were carried out in 250 mL beakers with 100 mL of the Cd^{2+} diluted stock solution and maintained under magnetic stirring at 300 rpm in a multiple-position hot plate stirrer (Velp Scientifica™ brand, AM4 model). Each treatment was repeated three times at a temperature of 293 K.

Before the adsorption tests, a species distribution diagram was made using the free software Chimera (Spana format).[108,109] This diagram was used to identify the pH range where cadmium would remain solubilized and available for adsorption onto biochar. This study did not explore the relationship between pH and the percentage of removal. A test was performed to determine the optimum adsorbent dose. This dose was selected after relating the adsorbent mass and its adsorption capacity (q$_e$). To study the effect of adsorbent dosage, different amounts of BCCPH (0.1, 0.5, 1.0, 1.5, 2.0, 2.5 and 3.0 g) were added to 100 mL of a 100 mg/L Cd^{2+} solution and kept in agitation at 300 rpm for 60 min, periodically readjusting the pH to 5 by adding HCl (0.1 M). Finally, each sample was filtered using qualitative filter paper (Hawach

Scientific 2.5 μm) and acidified with concentrated HNO_3. The quantification of the remaining Cd^{2+} of the solution after the adsorption process was carried out in a PerkinElmer Atomic Absorption Spectrometer, AAnalyst 400 model, and grade 2.5 AA acetylene gas as flame fuel (Table S6).

The q_e, (mg/g) and removal rate (Rr, %) were calculated according to Equations 7 and 8, respectively. Through the dose effect experiment, the amount of BCCPH with the best adsorption performance for Cd^{2+} was selected.

$$q_e = \frac{(C_o - C_e) \times V}{W} \qquad \text{(Equation 7)}$$

$$\%Rr = \frac{(C_o - C_f)}{C_o} \times 100 \qquad \text{(Equation 8)}$$

In Equations 7 and 8 C_o and C_e represent the initial and equilibrium concentration of Cd^{2+} in mg/L, V is the volume of the solution in L, and W is the mass of BCCPH in grams.[73] The values obtained were plotted as a function of the adsorption percentage versus the adsorbent mass and the point where the adsorption capacity (q_t) becomes constant was determined.

Kinetic and equilibrium experiments

For the adsorption kinetic studies, 1.5 g of BCCPH was added to 100 mL of a 100 mg/L solution of Cd^{2+} to evaluate the adsorption process as a function of time (5, 15, 30, 45, 60, 120 and 180 min) at 293 K. The points t = 0, $q_{t = 0}$ = 0 were added as the kinetic data to model the initial adsorption stage.[110]

The study of the adsorption isotherms was performed by adding 1.5 g of biochar to 100 mL of a Cd^{2+} solution at different concentrations (5, 25, 50, 100, 150, 200, 300 mg/L) in 250 mL beakers, stirred constantly at 300 rpm during 120 min. The procedure was the same as the adsorption kinetics and the points C_e, t = 0 and $q_{e(t = 0)}$ = 0 were added as the equilibrium data to model the initial adsorption step.[110]

Kinetic and equilibrium models of adsorption

A detailed explanation of the mathematical models used to describe the adsorption process can be found below.

As per the study of Weber (1984),[111] the adsorption process on porous adsorbents involves four steps. Therefore, experimental data is analyzed with different adsorption kinetic models based on these mass transfer steps during the solid-liquid sorption process.[96] The above mentioned steps can be described as follows:

(i) *The first step (bulk transport)*: the adsorbate is *rapidly* transported in solution after introducing the adsorbent, making it an insignificant step in process control.

(ii) *The second step (external or film diffusion)*: adsorbate ions *slowly* diffuse from the liquid phase to the adsorbent surface through a boundary film. This step was studied using the mathematical expressions (Equations 9 and 10) of Boyd et al. (1947)[112] and Reichenberg (1953).[113]

$$B_t = \pi \times \left[1 - \sqrt{1 - \frac{\pi}{3} \times \frac{q_t}{q_e}} \right]^2 ; \text{ for } \frac{q_t}{q_e} < 0.85 \qquad \text{(Equation 9)}$$

$$B_t = -\ln\frac{\pi^2}{6}\ln\left(1 - \frac{q_t}{q_e}\right) ; \text{ for } \frac{q_t}{q_e} > 0.85 \qquad \text{(Equation 10)}$$

where q_t and q_e are the amounts of cadmium ions adsorbed at a time *t* and an infinite time (equilibrium). The resulting slope of the plot B_t *vs. t* was used to calculate the value of B necessary for the subsequent determination of the coefficient of effective diffusion, D_i (cm^2/s), using Equation 11:

$$B = \frac{\pi^2 \times D_i}{r^2} \qquad \text{(Equation 11)}$$

where D_i is the effective diffusion coefficient of the adsorbate, and r the adsorbent particle radius that is considered to be spherical.

This model leads to the determination of diffusion processes as probable steps of limiting or controlling the mass transfer of the adsorption process. If the plot is linear and passes through the origin, the process is controlled by intraparticle diffusion. If the plot is linear but does not pass through the origin, the external diffusion or both external and intraparticle diffusion govern the overall rate of the sorption process. Also, the effective diffusion coefficient's value helps to distinguish between intraparticle diffusion and external diffusion. If D_i is in the range of 10^{-6} - 10^{-8} cm^2/s, it would be external diffusion, but if D_i is in the range of 10^{-11} - 10^{-13} cm^2/s, it indicates intraparticle diffusion or pore diffusion.[114]

(iii) *The third step (intraparticle diffusion):* adsorbate ions are *slowly* transported from the external surface of the adsorbent toward their pores. This step was studied using the Weber-Morris model[115] which is expressed as follows:

$$q_t = k_p \times \sqrt{t} + C \qquad \text{(Equation 12)}$$

where k_p (mg/g $\times$ min$^{1/2}$) is the intraparticle diffusion rate constant obtained from the slope and C (mg/g) is a constant associated with the thickness of the boundary layer obtained from the intercept of the plot of q_t *vs.* $t^{1/2}$. A higher value of C corresponds to a greater effect on the boundary layer.[116] This model assumes that if the straight line passes through the origin, the process is controlled by diffusion in the pores. However, if the plot fails to maintain linearity and the curve exhibits multiple straight lines, it may indicate that external diffusion and pore diffusion seem to happen simultaneously in the adsorption process. If the approximate values of the intraparticle diffusion rate constant follow the decreasing order of $k_I > k_{II} > k_{III}$, it is suggested that intraparticle diffusion occurs during the initial period (0-5 min) and the equilibrium of the intraparticle diffusion in the pores is reached in this period (step I). Then (steps II and III), the equilibrium of the intraparticle diffusion in the pores is broken and some cadmium ions in the solution can subsequently move to the pores.

It is important to mention that according to Wang & Guo (2022),[110] "the mass transfer step revealed by the intraparticle diffusion model is the diffusion of the adsorbate in the pores inside the adsorbent. The intraparticle model cannot study other multiple mass transfer processes."

(iv) *The fourth step (adsorption on active sites):* once the intraparticle diffusion equilibrium has been reached in the pores, the cadmium ions in the pores within the adsorbent are *rapidly* transferred to the active sites. This stage was studied through Ritchie kinetics[117] describing adsorption on active sites on heterogeneous surfaces energetically, where an ion or molecule may occupy n active sites. Ritchie's kinetics[117] is represented by Equation 13 for $n \neq 1$ (Ritchie nth-order) and by Equation 14 for $n = 2$ (Ritchie second-order, RSO):

$$q_t = q_e - q_e \times [1 + (n-1)\alpha t]^{\frac{1}{1-n}} \qquad \text{(Equation 13)}$$

$$q_t = \frac{\alpha \times q_e \times t}{1 + \alpha \times t} \qquad \text{(Equation 14)}$$

where q_t and q_e are the adsorption capacity (mg/g) at a time t and at equilibrium, respectively. The parameter n corresponds to the number of active sites that can be occupied by the adsorbate and α (g/mg/min) is the rate constant.

In addition to the previous models, which are established on solid physical grounds, the experimental data were analyzed using empirical models, that is, mathematical formulas that do not correspond to any specific physical model, but which are widely applied and reported in the scientific literature such as pseudo-first-order (PFO), pseudo-second-order (PSO), and Elovich models. The PFO model, which has been widely used to describe kinetic processes of pure physical adsorption and in a non-equilibrium state, can be represented by Equation 15.[118]

$$q_t = q_e (1 - e^{-k_1 \times t}) \qquad \text{(Equation 15)}$$

The parameter k_1 (1/min) can describe how fast the adsorption equilibrium is reached.[119] Important observations on PFO kinetics are:[96] a) the initial stage of adsorption should be modeled instead of modeling the overall adsorption process, b) there should be a high initial concentration of adsorbate, c) the adsorption process occurs predominantly in the initial stage where the fraction of active sites occupied approaches zero, d) the adsorbent material has a few occupied active sites possibly because they are not available or accessible, and these do not control adsorption. Therefore, the PFO model in some cases could represent external and internal diffusion processes.

The kinetics of PSO assumes that the limiting rate step is due to chemical adsorption involving the participation of electrons through ionic exchanges, transfer or formation of covalent or coordination bonds; it can be represented by the integrated form of Equation 16.[120]

$$q_t = \frac{k_2 \times q_e^2 \times t}{1 + k_2 \times q_e \times t} \qquad \text{(Equation 16)}$$

where k_2 (g/mg/min) corresponds to the constant used to describe the rate of the adsorption equilibrium.[119] According to studies,[121,122] some considerations should be taken into account regarding the PSO model: a) in the final step of the adsorption process the fraction of active sites occupied in the adsorbent is abundant and increases over time, and b) adsorption on active sites is the main mechanism and the step controlling the rate of the adsorption process, c) the initial concentration of adsorbate is low.

Elovich kinetics is commonly used to describe the chemical adsorption processes that occur in adsorbents with heterogeneous surfaces; it can be represented by Equation 17.[123]

$$q_t = \frac{1}{\beta} \times \ln(1 + \alpha \beta t) \qquad \text{(Equation 17)}$$

where α (mg/g $\times$ min) is a constant related to the initial rate[82] or the rate of chemisorption[124] and the constant β (mg/g) is related to the surface coverage (or desorption) during any one experiment. This kinetic equation involves the active sites being heterogeneous in terms of their

nature and activation energy; this implies a variation of the energy of chemisorption with the degree of surface coverage; specifically, the activation energy increases with the adsorption time.[124]

In general, the experimental data were analyzed through 14 kinetic models, reporting only those that met three requirements for the most appropriate model selection: **1.** The values of q_e experimental and q_e calculated are close to each other ($\Delta q_e < 0.35$). **2.** The adjusted R^2 value is about 1 or > 0.900. **3.** The value of Chi^2 is close to zero ($Chi^2 < 0.12$). The nonlinear regression method was used for the other models except for the Boyd and Weber-Morris models. This method was more precise at solving adsorption models than the linear regression method because the variables do not change during the solution process.[125–127]

The models of Langmuir (Equation 18),[128] Freundlich (Equation 19),[129] and Redlich-Peterson (Equation 20),[130,131] in their nonlinear forms, were used to fit the adsorption isotherms. The linear forms of the equilibrium models were used. However, the bias between the q_e values calculated from the experimental data and those estimated from the models was increased. For this reason, these fits are not shown here.[82,132]

$$q_e = \frac{K_L \times Q_{max} \times C_e}{1 + K_L \times C_e} \qquad \text{(Equation 18)}$$

$$q_e = K_F \times C_e^n \qquad \text{(Equation 19)}$$

$$q_e = \frac{q'_{mon} \times b_{RP} \times C_e}{1 + b_{RP} \times C_e^\alpha} \qquad \text{(Equation 20)}$$

In these equations, q_e and C_e represent the amount of adsorbate (Cd^{2+}) uptake at equilibrium (mg/g) on BCCPH and the adsorbate concentration at equilibrium (mg/L), respectively. Q_{max} is the maximum adsorption capacity (mg/g) and q'_{mon} represent the saturated mono-layer adsorption capacity (mg/g). The constants related to the affinity between an adsorbent and adsorbate: K_L (L/mg), K_F [mg/g/(mg/L)^n] and b_{RP} (L/mg) correspond to Langmuir, Freundlich and Redlich-Peterson, respectively. The exponent n (dimensionless) indicates the magnitude of the adsorption driving force or the surface heterogeneity and is not affected by the units of C_e and q_e. If $n = 0$ it suggests irreversible adsorption (horizontal plot) but if $n = 1$ it yields a linear plot, while $n \neq 1$ yields a nonlinear plot. Adsorption is favored when $n < 1$ (concave shape) and unfavorable when $n > 1$ (convex shape).[133] The value of the exponent α (dimensionless) must lie between 0 and 1. This study adopted an α correct value (to be shown later) using linear regression analysis with an adjusted $R^2 > 0.900$ and a weight of $Chi^2 < 0.3$.

The statistical bias of linearized equations raises questions about linear models' effectiveness in capturing the adsorption process's true nature on porous materials such as biochar. Possible factors contributing to this bias may be: 1. Linearization of equilibrium isotherms may introduce distortions in the data's structure due to alteration of the error distribution and affect the relationship between variables. For example, if a logarithmic transformation is used to linearize a nonlinear relationship, errors may propagate differently on the logarithmic scale than the original scale. 2. Adsorption on porous materials may be subject to nonlinear phenomena (i.e., surface heterogeneity) and non-ideal behaviors (i.e., interactions between adsorbate particles, diffusion effects, formation of multiple adsorbed layers; among others) which linear models do not adequately capture. 3. Sensitivity to experimental conditions, the linear models often require that errors meet certain assumptions: independence from each other, same probability distribution, and that they follow a normal distribution; necessary assumptions that may not be fully met in experimental conditions of adsorption on porous materials. Previous literature has shown that nonlinear models can provide a better description of adsorption processes and avoid statistical biases associated with linearization.[134–136] The cited studies provide convincing evidence that nonlinear regression should be preferred. Nonlinear models appear to be able to capture the inherent complexity of the adsorption process because they can maintain data integrity and are not constrained by the need to linearize the relationship between variables, allowing them to represent a wider variety of adsorption curve shapes. Thus, nonlinear regression is a more robust and reliable tool for modeling the adsorption process in porous systems.[137]

Additionally, the separation factor or equilibrium parameter R_L was calculated, according to:[138]

$$R_L = \frac{1}{1 + K_L \times C_o} \qquad \text{(Equation 21)}$$

where R_L is the constant separation factor (dimensionless) of the solid-liquid adsorption system, K_L is the Langmuir equilibrium constant, and C_o (mg/L) is the initial adsorbate concentration. If $R_L < 1$, a concave isotherm will be observed and the adsorption process will be favorable.[139]

Effect of temperature and estimation of thermodynamic parameters

For the evaluation of the effect of temperature on the adsorption process, 1.5 g of BCCPH were added to 100 mL of solution of Cd^{2+} (5, 25, 50, 100, 150, 200, 300 mg/L) at different temperatures (293, 308 and 323 K). The procedure was identical to the one described in the STAR Methods section for "kinetic and equilibrium experiments". For the determination of the thermodynamic parameters, K_c was first determined as the equilibrium constant derived from the Langmuir constant (K_L) multiplied by the molar mass of the adsorbate (Mm; g/mol), by 55.5 mol/L, and then by 1,000 (Equation 22).[140] Then, the Gibbs free energy of adsorption (ΔG) was calculated using Van't Hoff's equation (Equation 23), where R is the gas constant (8.314 J/mol K). The adsorption enthalpy (ΔH) and entropy (ΔS) were calculated by using the adsorption data at different temperatures (Equation 24). The values of ΔH and ΔS were calculated by means of the slope and intercept of the $\ln K_c$ vs. 1/T plot.[82,88]

$$K_c = K_L \times Mm \times 55.5 \times 1000 \qquad \text{(Equation 22)}$$

$$\Delta G = -RTlnK_C \qquad \text{(Equation 23)}$$

$$lnK_C = \frac{-\Delta H}{R} \times \frac{1}{T} + \frac{\Delta S}{R} \qquad \text{(Equation 24)}$$

Computational details

To gain a deeper understanding of the interaction of Cd^{2+} ions with biochar, the recently widely used DFT simulations were performed, combined with experimental studies to understand the mechanism of the adsorption process.[141–143] The initial structure of the carbonaceous surface model was generated using visualization software like Molden[144,145] and then optimized using the level of theory described in this section. The DFT simulations were performed by B3LYP (hybrid density functional). DFT-D3(BJ)[146] with the Becke and Johnson (BJ)-damped[147,148] dispersion correction was performed on B3LYP, which is important for the systems studied.[91,149] Regarding the basis set, the def2-TZVP[150,151] was used for calculations. It is an all-electronic basis set of C, H, O. At the same time, for the Cd atom, a pseudopotential replaces the 28 core electrons, and it is suitable for general quantum mechanical calculation of medium and large molecules. Moreover, the B3LYP-D3/def2-TZVP level of DFT calculation is suitable for balancing speed and accuracy.[151]

All calculations were carried out in this work using the Gaussian 16 software package.[141] The calculation process included geometry optimizations, vibrational frequency analysis, and single-point energy calculation. Geometry optimizations of the carbonaceous surface, free metal ion (Cd^{2+}), and their adsorbent complexes were calculated at the B3LYP-D3/def2-TZVP level of DFT in their ground states that corresponded to the minimum point on the potential energy surface, at 298 K and a pressure of 1.0 atm. The effect of water as a solvent was considered using the Implicit Solvation Model named the Integral Equation Formalism for the Polarizable Continuum Model (IEFPCM),[152] which was used to simulate the aquatic environment. The correct ground-state structure with the fewest spin impurities and lowest electron energy was determined by calculating the single-point energies of the starting structures in different electronic states.[89] Single-point energy is calculated at the B3LYP-D3/def2-QZVP//B3LYP-D3/def2-TZVP level of theory by adding zero-point energy (ZPE) and thermal (temperature-dependent) corrections. Adsorption energy (E_{ads}) of adsorbate "A" on the solid surface "B" can be calculated as follows (Equation 25):

$$E_{ads} = E_{AB} - E_A - E_B \qquad \text{(Equation 25)}$$

where E_{ads} is the adsorption energy, kJ/mol; E_A is the energy of the adsorbent, kJ/mol; E_B is the energy of the adsorbate (Cd^{2+}), kJ/mol; E_{AB} is the total energy of adsorbate/adsorbent system in the equilibrium state, kJ/mol. When E_{ads} is negative, the adsorption of the adsorbate is exothermic. Higher negative values of E_{ads} correspond to stronger adsorption.

QUANTIFICATION AND STATISTICAL ANALYSIS

Each experiment was conducted in triplicate. Data were plotted and statistically analyzed using OriginPro 2023 (Originlab Corporation, USA).[153] Tables were made using Microsoft Word and Excel 365 (Microsoft Corporation, USA).